NTNU – Trondheim
Norwegian University of
Science and Technology

Supported Iridium-Ruthenium Mixed Oxide Catalysts for Oxygen Evolution

Synthesis of Mixed Oxides by the Microwave
Polyol Method. Composition Dependency of
the Catalytic Activities of Mixed Oxides for the
OER in PEM Water Electrolysis

Espen Vinge Fanavoll

Materials Science and Engineering
Submission date: June 2013
Supervisor: Svein Sunde, IMTE
Co-supervisor: Magnus Thomassen, Sintef

Norwegian University of Science and Technology
Department of Materials Science and Engineering

Preface

This is a master thesis written in the spring of 2013, as the final part of the master program at the Department of Materials Science and Engineering, NTNU. The study has been done in collaboration with researchers at SINTEF Materials and Chemistry. At NTNU it is common to write the master thesis following a preliminary project of the same topic. This work is a continuation on the previous work, where the microwave polyol method was established as an advantageous method for producing supported iridium oxide in the laboratory. The work done in the preliminary project will be summarized in a section in the theory of this thesis.

This study seeks to extend the microwave polyol synthesis method to synthesis of supported ruthenium oxide and iridium-ruthenium mixed oxide catalysts. Furthermore, these catalysts will be examined in terms of composition and catalytic properties. Of particular interest is the composition dependency of the catalytic properties of mixed oxides, and the hypothesis that the total current should be a linear superposition of partial currents from each component.

I would like to extend my thanks to my supervisors, Prof. Svein Sunde and Magnus Thomassen for guidance during the project. Further thanks go to Per Erik Vullum and Luis Colmenares for their contributions and assistance with the experimental work in this thesis.

Trondheim, June 17, 2013

Espen Vinge Fanavoll

Abstract

In this work the microwave polyol synthesis method have been shown as an advantageous method for producing ATO supported IrO_2, RuO_2 and iridium-ruthenium mixed oxides, allowing for faster synthesis than the normal polyol method. Another advantage is high flexibility, allowing for synthesis of several batches of different compositions in parallel, while giving great control over each batch. For this work alone, several days of experimental work was saved, as the microwave synthesis method is several times faster than the normal polyol method.

Catalysts of iridium oxide, ruthenium oxide and three compositions of mixed oxides were synthesized by the microwave polyol method in this work. The composition and catalyst loading were found by EDS analysis. Catalyst loading was found to be at target values for all synthesis experiments in this study. The ruthenium contents of the mixed oxides were not up to target values. This may be due to experimental error; the synthesis observations indicate the method should yield full or near full reduction and deposition of the catalyst. The synthesized mixed oxides are dubbed atomically mixed oxides, as iridium and ruthenium atoms should be mixed at an atomic level. In addition to these, physically mixed oxides were produced by mixing pure iridium and ruthenium oxides to imitate the concentrations of the atomically mixed catalysts.

The catalysts were analyzed by voltammetry to examine the catalytic properties. The addition of even small amounts of ruthenium to mixed oxides was found to give a significant increase in catalytic activity. Catalysts containing particles of pure ruthenium oxide were found to have a loss of catalytic activity at electrode potentials above 1.45 V, due to further oxidation and dissolution of ruthenium. With regards to mixed oxide composition, the results follow closely to the relationship expected by assuming that the total current is a linear superposition of the partial currents of the components, supporting the hypothesis that interaction effects between ruthenium and iridium atoms are weak. Iridium oxide was found to have a stabilizing effect on ruthenium oxide when the two are atomically mixed.

Sammendrag

I dette arbeidet har mikrobølge-polyolmetoden vist seg som en fordelaktig syntesemetode for produksjon av ATO-bårne katalysatorer av IrO_2, RuO_2 og blandede oksider av iridium og ruthenium. Denne metoden tillater raskere synthese av kataysatorer enn den tradisjonelle polyolmetoden. I tillegg oppnår man større fleksibilitet og kontroll over syntesen, siden den tillater syntese av flere forskjellige oksidsammensetninger i paralell. Dette sparte flere dager med eksperimentelt arbeid i denne oppgaven.

Katalysatorer av iridiumoksid, rutheniumoksid og blandede oksider av ruthenium og iridium har blitt syntetisert i dette arbeidet. Sammensetningen og forholdet mellom katalysator og bærer ble analysert med EDS. Mengden katalysator ble funnet til å være nær målverdiene. Rutheniuminnholdet i de blandede oksidene var noe lavere enn målverdiene. Dette kan derimot være på krunn av eksperientell feil, da andre indikatorer viser at syntesemetoden gir full eller nesten full reduksjon og deposisjon av katalysatorpartiklene. I tillegg til de syntetiserte blandede oksidene, kalt atomisk blandede oksider, ble det preparert fysisk blandede oksider ved å kombinere de rene oksidene av iridium og ruthenium med samme sammensetning som de atomisk blandede oksidene.

Katalysatorene ble analysert med voltammetri for å finne de katalytiske egenskapene til prøvene. Små mengder ruthenium i blandede oksider viste seg å gi signifikant forbedring av den katalytiske aktiviteten. Prøver med partikler av ren rutheniumoksid hadde et aktivitetstap når elektrodepotensialet passerte 1.45 V, dette viser at ruthenium blir videre oksidert og løst opp. Når egenskapene ble analysert i forhold til sammensetning, viste resultatene at de ligger nær verdiene beregnet ut fra hypotesen om at totalstrømmen på katalysatoren er en lineær addisjon av bidrag fra komponentene i oksidene. Dette støtter hypotesen om at interaksjonen mellom de to elementene i oksidet er svak. Iridium ble funnet å ha en god stabiliserende effekt på rutheniumoksid når de to er i samme partikkel.

Table of Contents

1   Introduction

As the fossil energy sources society has come to depend on are inevitably depleting, new, renewable energy sources are sought. One of the main concerns is the need for an energy carrier for the transport sector and for storage of energy. Oil and gas are reliable and mobile energy carriers, able to be consumed by small, mobile engines when energy is needed. Renewable sources are often either stationary or dependent on external conditions, like wind or sunshine, so there will be a need for a reliable energy carrier, in order to utilize energy where and when it is needed. In order to be satisfactory, an energy carrier must not lead to significant energy losses. Consequently, processes for producing and consuming this carrier must be effective.

The hydrogen economy is one proposed solution to this problem. Hydrogen has the highest weight specific energy density of all the presently known fuels (142 MJ/kg), although in gaseous form the volumetric energy density is on the other end of the scale. There are three main processes in the hydrogen economy, each with its own technological and economic challenges: Production, storage and transport, and consumption of hydrogen. This study will focus on the first.
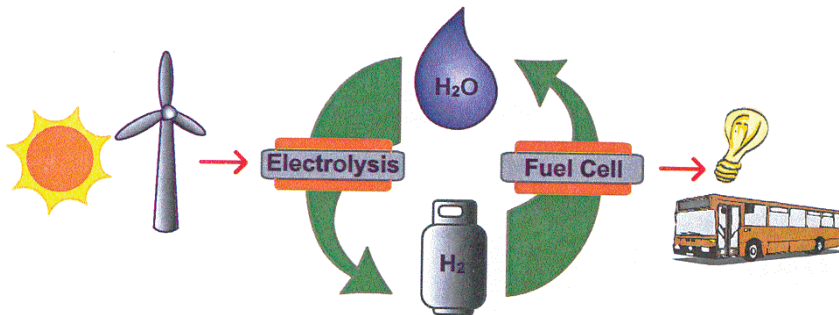

Figure 1.1: Illustration of the hydrogen production/consumption cycle in the hydrogen economy [1].

Hydrogen is the most abundant element in the universe. Here on earth the hydrogen is bound to oxygen in water, and to carbon in organic matter. Today almost all hydrogen production is in the form of hydrocarbon reforming, a process which has a low energy conversion efficiency [2], and produces carbon dioxide. In terms of sustainability, the ideal way to produce hydrogen would be by water electrolysis. Superficially, water electrolysis is a simple process; electricity is applied, splitting water molecules into their constituent elements: hydrogen and oxygen. A fuel cell does the opposite of an electrolyzer, converting the chemical energy back into electricity by reacting the hydrogen gas with oxygen from air. This cycle releases no pollutants, as the only product in the fuel cell is water, and the processes are very energy efficient [2]. The hydrogen gas produced by water electrolysis is also very pure, compared to the gas produced by hydrocarbons.

1 Introduction

Alkaline water electrolysis is currently the most used method of water electrolysis[2]. The advantages of this process are that the technology is well matured, and the materials used are relatively cheap. The biggest disadvantage is the low specific production rate, meaning large electrode areas, and thus large electrolyzer units, are required to produce hydrogen at sufficient rates. The PEM (Polymer Electrolyte Membrane) technology has a greater specific production rate than the alkaline process. Combined with the thin solid membrane, this means that PEM electrolyzers could be built more compact. Hydrogen may then be produced delocalized, in fueling stations or even homes, rather than just centralized.

A major concern with the PEM technology is the oxygen evolution reaction (OER) at the anode, which has a high overpotential[3], giving a large contribution to the cell voltage. As the major limiting factor for water electrolysis in general is the cost of electricity, any decrease in the cell voltage would be very beneficial. The anode conditions are acidic and highly oxidizing, so the stability of the catalyst is important. The catalyst showing the greatest activity is ruthenium oxide, but the high instability under these conditions limits its practicality. Iridium oxide has a lower catalytic activity than RuO_2, but shows a greater stability. By alloying iridium oxide with ruthenium, the catalytic activity will increase, but this will come at the cost of lower stability. Alloying with other elements, like tantalum or tin would increase the stability and decrease the cost of the catalyst.

The common synthesis method for the iridium and ruthenium catalysts in the laboratory is the normal polyol synthesis. This method is not very fast, and an alternative is sought. In the preliminary project to this work the microwave polyol method was established as a synthesis method for ATO supported iridium oxide [4]. Different synthesis parameters were explored, and the synthesis method showed great potential. The biggest advantage is the ability to synthesize more catalysts with different parameters faster that for the normal polyol method.

The first objective of this study is to extend the microwave polyol method to include ruthenium oxide and mixed oxides, and examine the properties of these catalysts.

The relationship between catalytic properties and composition of mixed oxides of ruthenium and iridium has been studied before with differing conclusions [5, 6]. The second objective of this study is to examine this relationship for supported mixed oxide particles synthesized by the microwave polyol method.

2   Theory

2.1   Water electrolysis

Water electrolysis is an old and relatively simple reaction. A DC voltage is applied to an electrolyzer, splitting the water molecule into oxygen and hydrogen (Eq. 1). standard potential is 1.229 V[7]. The reaction is endothermic, and consumes heat. The thermoneutral voltage, where the cell operates adiabatically, is 1.47 V.

$$\text{Total reaction} \qquad 2H_2O \rightarrow O_2(g) + 2H_2(g) \qquad\qquad (2.1)$$
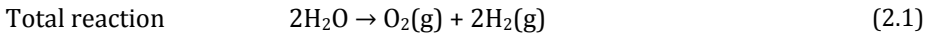
The reversible voltage can be calculated from the standard potential and the reaction conditions by the Nernst equation[8]:

$$E_{rev} = E^0 - \frac{RT}{nF} \ln \frac{a_{red}}{a_{ox}} \qquad\qquad (2.2)$$

Electrolysis reactions are not operated at reversible voltage. The total cell voltage will be the sum of the reversible voltage, anodic and cathodic overpotential, and IR losses from electrical resistance in the cell, as given by equation (2.8)[8].

$$E_{cell} = E_{rev} + |\eta_a| + \eta_c + IR \qquad\qquad (2.3)$$

The advantages of producing hydrogen by water electrolysis are the ability to produce a very high purity, with oxygen as the only by-product, and very high availability of the raw materials. The main drawback is that the cost of electricity is presently too high for water electrolysis to be cost effective compared to hydrogen production from fossil sources. A few large scale electrolyzers exist in places with excess electrical power or low cost [2].

While the most common large scale water electrolyzer is the alkaline electrolyzer[2], the low current densities and energy loss from overpotential[7] drives the search for a new electrolyzer. The PEM water electrolysis technology, developed from PEM fuel cell technology, is the main contender.

2.1.1   PEM water electrolysis

The PEM water electrolyzers use a polymer electrolyte, typically Nafion, separating the anode and cathode. On the anode, water is consumed to create oxygen gas, protons and electrons. The electrons flow through the external circuit, while the protons are conducted through the polymer membrane. At the cathode, protons recombine with electrons to form hydrogen gas. The half-cell reactions are given below [3]:

Cathode reaction: $4H^+ + 4e^- \rightarrow 2H_2$ (2.4)

Anode reaction: $O_2 + 4H^+ + 4e^- \leftarrow 2H_2O$ (2.5)
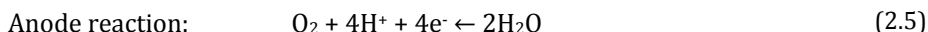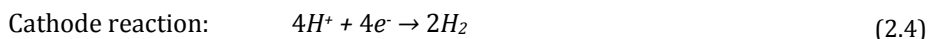
Because the oxygen-producing anode and hydrogen-producing cathode are physically separated by the polymer membrane, the product hydrogen is very pure. Hydrogen gas of 99.999% purity may be produced [9]. Figure 2.1 shows a simplified schematic of the PEM electrolyzer cell.
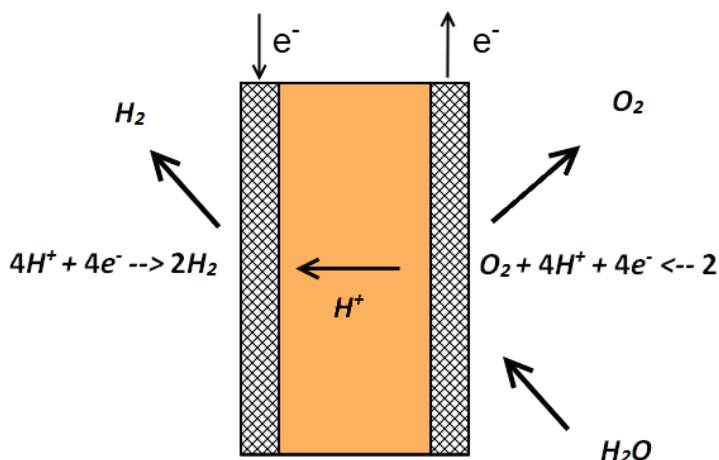

Figure 2.1 Simplified schematic of the PEM cell.

High current densities are obtained in PEM electrolysis cells. Current densities of 1 A/cm^2 have been achieved at 1.6 - 1.7 V, while for alkaline cells 0.2 A/cm^2 are observed at 1.7 - 2.0 V. Current densities of 3 - 5 A/cm^2 are reported as possible without applying excessive voltages[10]. The excellent performance is due to low overpotentials, low IR loss due to the thin polymer membrane, and fast transport mechanisms due to efficient cell design [7].

The challenge with PEM electrolyzers is that the anode reaction has a large overpotential, which means a higher voltage is needed to produce hydrogen at acceptable rates. This lowers the energy efficiency of the whole system, as the excess energy is dissipated as heat.

2.2   Catalyst for the oxygen evolution reaction

In order to reduce the overpotential from the oxygen evolution reaction, a catalyst may be applied to the anode. Due to the highly oxidative conditions at the anode, oxides are the most suitable catalyst materials. The performance of any catalyst depends on the reaction mechanism taking place.

Several different mechanisms for the oxygen evolution reaction have been proposed by Matsumoto and Sato [11] and Trasatti [12]. One probable reaction mechanism is as follows [10]:

In the first step water reacts at a catalyst surface site to form adsorbed OH-groups (S represents an active surface site):
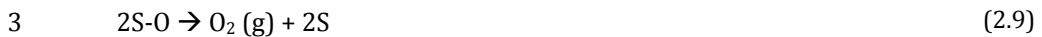
1. H_2O (l) + S → S-OH + H^+ + e^- (2.6)

This is followed by either the oxide path:

2a   2S-OH → S-O + S + H_2O (2.7)

or the electrochemical oxide path:

2b   S-OH → S-O + H^+ + e^- (2.8)

Both paths end with desorption of oxygen from the surface:

3   2S-O → O_2 (g) + 2S   (2.9)

The reaction mechanism involves adsorbed oxygen atoms on the catalyst surface, and it has been found that the catalytic activity of is dependent on how strongly oxygen bonds with the surface sites. Trasatti [12] has examined many conductive oxides, and evaluated their catalytic activity for the oxygen evolution reaction. Figure 2.2 shows a volcano plot of several oxide electrodes. The catalytic activity, represented by the overpotential η at a given production rate, is dependent on the heat of adsorption of oxygen atoms on the catalyst surface. Too weak adsorption leads to slow adsorption and fast desorption, giving low coverage on the surface. Too strong adsorption limits the rate of the surface reactions. This is known as Sabatier's principle [13]. To achieve the optimal production rate an intermediate value for the heat of adsorption is required, which is shown by the top of the "volcano". Other factors have been shown to act as the descriptor, the term on the x-axis of the plot, for catalyst volcano plots, though they are generally related in some way to the binding energy of reaction intermediates[14].
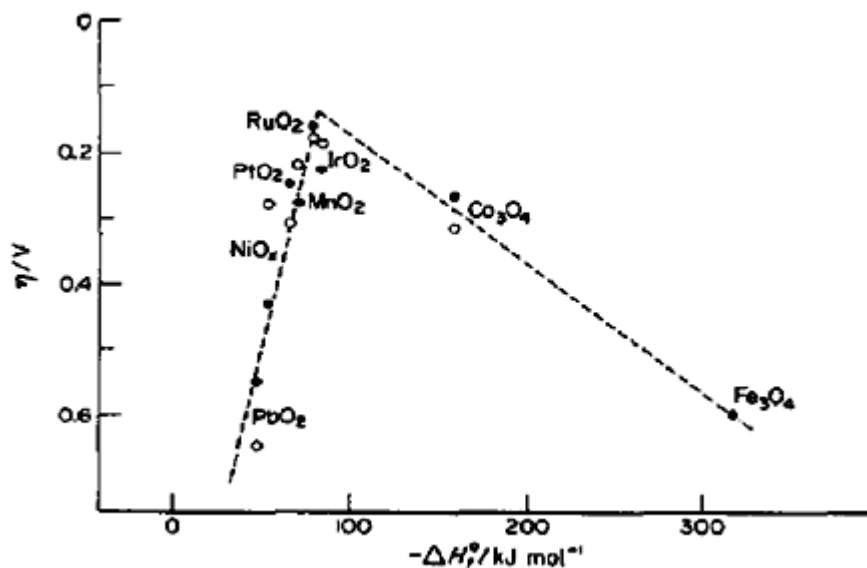
Figure 2.2: Volcano plot, with the overpotential at a certain current as a function of the heat of adsorption of oxygen atoms on the catalyst surface [12].

The catalyst with the highest activity is ruthenium oxide, but the oxide becomes unstable at higher potentials, leading to a lower catalyst lifetime. Iridium has been proven to be more stable than ruthenium, and will also have a stabilizing effect on ruthenium in an alloy catalyst [15]. This will be discussed in greater detail in section 2.4.

Some studies concentrate on finding alternatives to iridium and ruthenium oxides as catalysts, using more abundant materials. Suntivich at al. [16] have utilized theoretical calculations based on density functional theory to find optimized perovskite oxide compositions for the OER. Any advances in iridium-based catalysts must be measured up against the alternatives.

In order to utilize the most of the expensive catalyst materials, it is useful to increase the active surface area. Therefore, a support material, for example antimony tin oxide (ATO), is used. The support stabilizes small catalyst particles, with large specific surface areas, and prevents agglomeration.

2.3   Electrochemical characterization

Cyclic voltammetry and linear sweep voltammetry are the most common voltammetric methods for investigating catalytic properties[17]. Both methods require creating a working electrode with the catalyst and applying a voltage in an electrochemical cell with an aqueous electrolyte using a potentiostat. The potential at the working electrode is measured against a reference electrode.

2.3.1   Cyclic voltammetry

In cyclic voltammetry (CV), the applied voltage is changed at a constant sweep rate, v, within an interval using a potentiostat, while measuring the current response. The potential waveform is illustrated in Figure 2.3. The interval limits typically lie between the potentials for hydrogen and oxygen evolution.
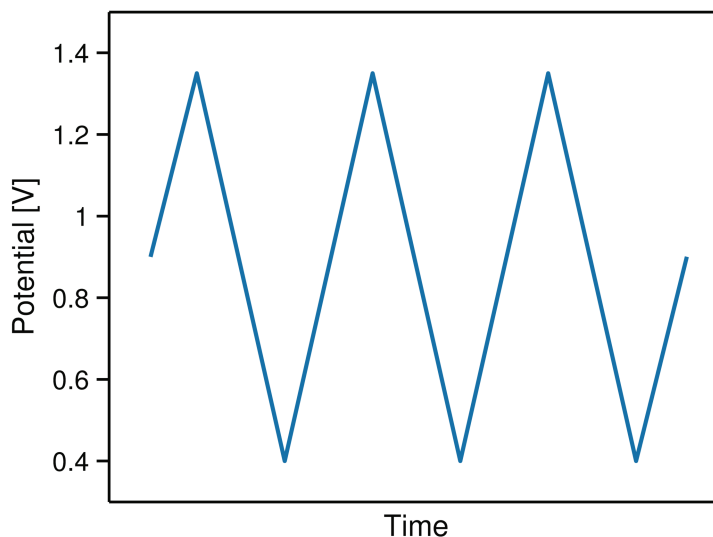

Figure 2.3: Potential waveform during cyclic voltammetry

In the cyclic voltammogram, a plot of the current as a function of potential, current peaks with height I_p can be observed, corresponding to certain surface reactions. The peak current increases with increasing sweep rate. If the surface reaction is slow, the peak potential will be dependent on the sweep rate. A fast surface reaction will be indicated by a peak potential that is independent on the sweep rate. Positive currents are denominated anodic currents, while negative currents are cathodic[8].

Figure 2.4 shows a typical voltammogram for iridium black, illustrating the effect of increasing sweep rate on the peak currents and the area of the voltammetry curves. The peaks correspond to adsorption and desorption of protons, by reaction (2.10):
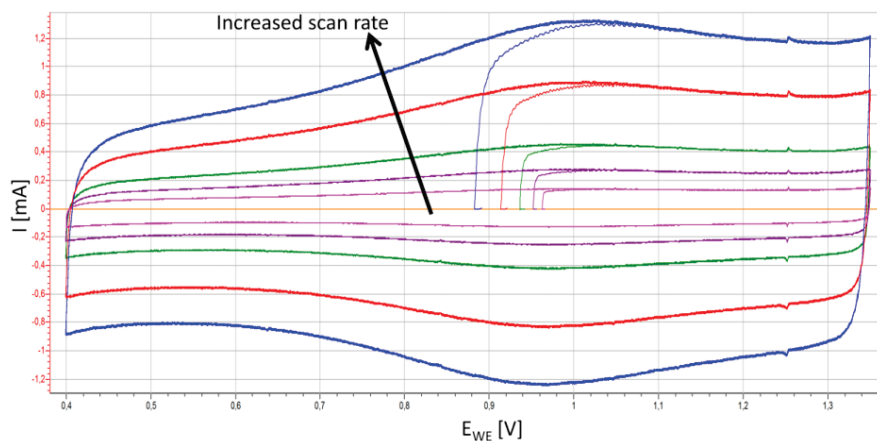
$$IrO_a(OH)_b \rightleftharpoons IrO_{a+\delta}(OH) + \delta H^+ + \delta e^- \tag{2.10}$$

Figure 2.4: Cyclic voltammogram of iridium black for different sweep rates [18].

2.3.2   Linear sweep voltammetry

Linear sweep voltammetry is a technique used to obtain polarization curves. LSV involves slowly increasing the potential at the working electrode at a constant rate, as illustrated by Figure 2.5, while measuring the current. Using a slow sweep rate ensures the reaction conditions on the surface are near steady-state[17].
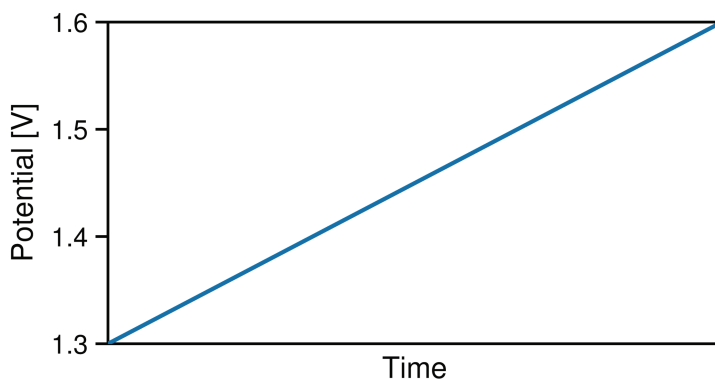

Figure 2.5: Voltage-time plot for linear sweep voltammetry of an oxygen electrode.

A common way of presenting the data from linear sweep voltammetry is the Tafel plot, in which the potential is plotted against the logarithm of the current density. The Tafel equation [8] is given below:

$$\eta \; = \; a \; + \; b \log |i| \; = \; b \log \left| \frac{i}{i_0} \right| \tag{2.11}$$

The constant b is the Tafel slope, and the constant i_0 is the exchange current density, which is the current density at zero overpotential. A good catalyst will have a low Tafel slope and/or a high

exchange current density, meaning the overpotential when operating at higher current densities will be low. The slope is also a major parameter in determining the kinetics of the reaction, as the Tafel slope is an intensive parameter, only dependent on the reaction mechanism[12]. Tafel slopes can be calculated theoretically from proposed reaction mechanisms [19] and compared to experimental values. The magnitude of *b* is given in equation below:

$$b = \frac{-2.303RT}{\beta n F} \tag{2.12}$$

By extrapolating the data to zero overpotential, the exchange current density, i_0, may be found. This is the current for the reaction at the reversible potential. The exchange current density is an extensive property, dependent on several factors, like electrolyte concentration and electrode surface morphology [8]. This makes performing voltammetry at constant conditions essential for producing comparable results for analysis.

2.3.3 *Accelerated stability testing*

Accelerated stability testing is basically a cyclic voltammetry technique with the intention of degrading the catalyst. The technique scans the potential more rapidly, and the upper potential limit is higher than the standard CV cycling, in order to promote degradation in a limited amount of time. When the technique is combined with linear sweep voltammetry run directly before and directly after the AST, a measure of the stability of the catalyst can be seen by comparing the Tafel plots.

2.3.4 *Normalization*

In order to compare catalysts, it is useful to normalize the currents with regards to the surface area available. Doing this, one may compare catalyst activity free of other variables like the particle surface area and catalyst loading, parameters that may be significantly different for different catalysts.

By integration of the positive-current part of the cyclic voltammogram, with regards to time instead of potential, a charge $q*$ is acquired[12]. In theory, the charge obtained from a voltammogram of infinitely fast sweep rate is related to the reaction happening on the very surface, and is thus proportional to the available surface area. This charge is denominated the outer charge, or surface charge, q_s*. The charge acquired from a voltammogram of infinitely slow scan rate gives enough time for the protons to diffuse into less accessible areas, like pores and along grain boundaries[20]. This is called the total charge, denominated q_T*. The difference between the total charge and the outer charge yields the inner charge, q_i*.

The charge has been shown in some cases to be inversely proportional to the square root of the sweep rate [20]. This is due to proton diffusion into the bulk of the particle. A plot of the charge as a function of the inverse of the square root of the sweep rate, q vs. $1/\sqrt{v}$, should give a straight

line, as shown in Figure 2.6. By extrapolating the linear function to the intersection with the y axis ($v \rightarrow \infty$), the outer charge may be found.
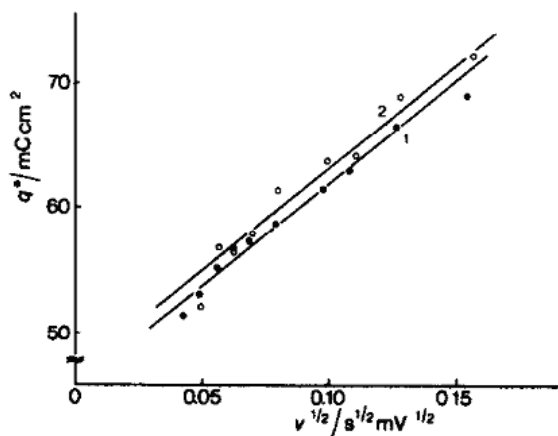

Figure 2.6: A typical plot of charge as a function of the inverse of the square root of the sweep rate. Values 1 and 2 are for $HClO_4$ and KOH electrolytes respectively, for a RuO_2 electrode [20].

Similarly, a plot of the inverse of the charge as a function of the square root of the sweep rate should yield a linear function, as seen in Figure 2.7. By extrapolating this function to the intersection with the y axis the total charge is found.
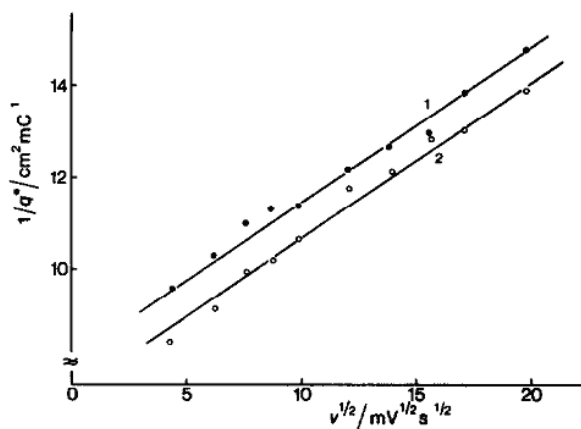

Figure 2.7: A typical plot of the inverse of the charge as a function of the square root of the sweep rate. Values 1 and 2 are for $HClO_4$ and KOH electrolytes respectively, for a RuO_2 electrode [20].

It has, however, been shown by previous work on iridium oxide catalysts [18] that the linear relationships above may not be present in practice. This could well be due to the small size of the catalyst particles, so that the diffusion limitations are not present at most sweep rates. The

charge recorded at higher sweep rates will however still be related to the surface area, and give some reference point for normalization of the currents. The charge at 300 mV/s will be used as such in this work.

2.3.5 Correcting for cell resistance

During electrochemical characterization there are some contributions to the measured potential not directly related to the oxygen evolution reaction. As there is a significant distance between the electrodes in the test cell, the cell resistance is significant, and must be accounted for. One way to compensate for this is to fit the constants equation (2.13) to the experimental data:

$$E = a + b \log|i| + |i|R \qquad\qquad (2.13)$$

This is basically the Tafel equation (2.11) with the addition of a term including a contribution to the potential from cell resistance, which increases linearly with the current density, as per Ohm's law.

Figure 2.8 shows how iR correction has been used by Owe et al. [5] to correct for the cell resistance from linear sweep measurements on pure unsupported iridium oxide. The corrected data extends the linear region, where the current is too low for cell resistance to have an impact, into higher current densities.
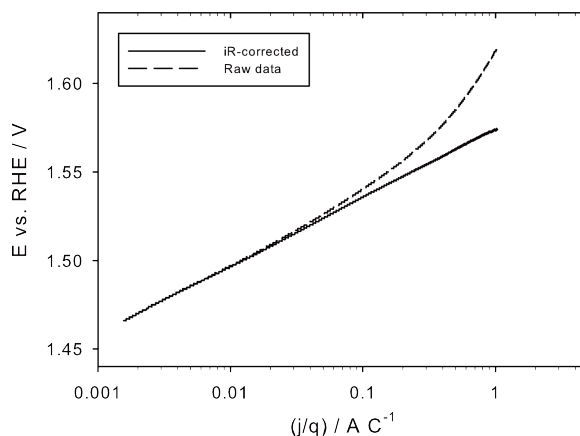

Figure 2.8: Example of iR correction of a Tafel curve. Data collected at 5 mV/s for a pure iridium oxide sample [5].

2.4 Properties of catalysts for the oxygen evolution reaction

With knowledge of electrochemical characterization of catalysts, different catalyst materials and compositions can be examined in terms of their performance. The two most important performance criteria are catalytic activity and catalyst stability. Catalytic activity can be quantified as the current at a given potential or the potential at a given current. Stability can be quantified from the change in catalytic activity over time, like before and after AST cycling.

This study focuses on the properties of catalysts of iridium and ruthenium oxides, and mixes and these, supported by ATO. Of significant interest is if iridium and ruthenium atoms interact with each other, and how the properties depend on the composition of the catalyst oxide. If there are no atomic interactions between iridium and ruthenium in mixed oxides, one would expect the total reaction current on the catalyst to be a linear superposition of the two constituent elements. The total current density at a given potential may then be calculated by equation (2.14).

$$i_{tot} = x_{Ru} * 10^{\left(\frac{E-a_{Ru}}{b_{Ru}}\right)} + (1 - x_{Ru}) * 10^{\left(\frac{E-a_{Ir}}{b_{Ir}}\right)} \qquad\qquad (2.14)$$

x_{Ru} is the atomic percentage ruthenium in the catalyst, a and b are the constants in the Tafel equation (2.11).

If there is, however, an interaction between the noble metals in the oxide one would expect the result deviating from the sum of its parts.

For metallic films used in catalysis the agreed theories state that metallic atoms in thin films interact with each other, via electronic interaction of the orbitals. This is described by density functional theory, in the Hammer-Nørskov *d*-band model [21-23]. For instance has it been shown that the adsorption energy of CO on noble metal thin films is dependent on the number of layers [24]. The number of layers determines lattice effects influencing electronic effects on the surface.

Whether the effects in metallic catalysts also hold true in catalytic oxides is conflicted. Kötz and Stucki [6] produced sputtered electrodes of varying composition, and found that iridium causes a drastic loss in the corrosion rate of the catalyst, at a cost of lowered catalytic activity. The study found that the potential of the oxygen evolution reaction at a current density of 0.1 mA/cm^2 increased linearly with increasing iridium content, as seen in Figure 2.9. The dashed line is calculated with the assumption that the total reaction current is a linear combination of currents from IrO_2 and RuO_2, the previously expected relationship between the properties and the composition.
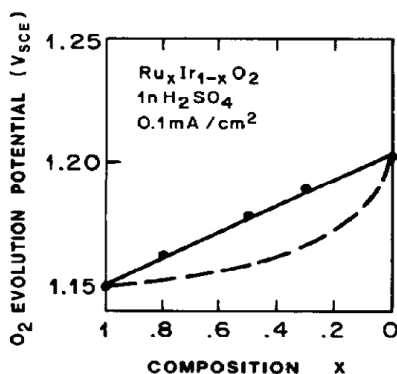
Figure 2.9: Potential for the OER at a current density of 0.1 A/cm² as a function of the composition. The dashed line represents linear addition of the contributions to the current from IrO₂ and RuO₂.

Kötz and Stucki concluded that the observed result is due to a common band formation between the two oxides, which helps stabilizing the RuO_2 and preventing it from being oxidized to RuO_4.

Owe et al. [5] explored the properties for unsupported particles of iridium and ruthenium oxides. The study considered both atomically mixed catalysts, meaning the precursors are synthesized together and are present in the same particles, and physically mixed catalysts, meaning pure iridium and ruthenium oxides were mixed to imitate the compositions of the atomically mixed catalysts. Catalyst mixes of 25, 50 and 75 at% ruthenium were created. Particles were synthesized by hydrolysis and heat treated in air. Average particle sizes after heat treatment were found to be in the range of 16 to 26 nm. Bulk composition was measured by EDS, and surface composition was measured using XPS.

The composition measurements showed that the particle surfaces of the atomically mixed oxides were enriched in iridium, meaning the effective ruthenium content in the catalyst is reduced. Figure 2.10 shows the polarization measurements performed on a selection of the catalysts. Note that the mixed oxides are target 50 at% ruthenium, and the measured surface concentration is lower. As expected, the pure ruthenium oxide sample has the highest activity, and the pure iridium oxide has the lowest. Of the mixed oxide catalysts, the physical mix has a higher activity than the atomic mix. This is as expected, as the surface ruthenium content will be significantly lowered in the atomic mix. Figure 2.11 shows the potential required for the OER at a charge-normalized, iR corrected current of 10 mA/C. This result deviates significantly from the results of Kötz and Stucki (Figure 2.9), as the potentials are much closer to what would be expected for a superposition of the current contributions, as per equation (2.14). This means that interactions between iridium and ruthenium are weaker than what was shown for the sputtered thin films above.
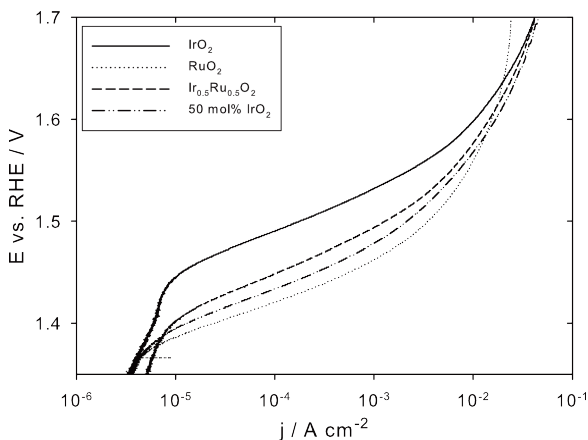
Figure 2.10: Polarization curves recorded at 50 mV/s for pure oxides and a physical and atomic mix with target 50 at% ruthenium.[5]
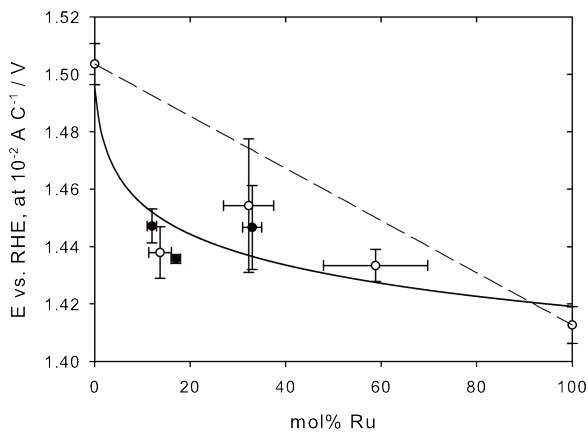

Figure 2.11: Potential required for an iR-corrected normalized current of 10 mA/C as a function of the ruthenium content. Filled squares are atomic mixes and circles are physical mixes and pure oxide catalysts. The solid line is the potential calculated by assuming the total current is the sum of partial currents of the two oxides.[5]

2.5   Normal polyol synthesis

The normal polyol synthesis method is a well-known and widely used method to synthesize noble metal nanoparticles. Both supported and unsupported catalysts may be produced. The method can be utilized to synthesize Pt, Rh, Pd, Ir, Au and Ag with small particle sizes and narrow size distributions [25]. Catalytic properties of metal catalyst depend strongly on the active surface area of the particles, and smaller particles lead to a higher fraction of the catalyst atoms to be located on the surface. In addition, particle agglomeration decreases the available area, so the particles must be stabilized to avoid this.

Polyol synthesis using ethylene glycol (EG) as the polyol has shown great results for many noble metals [25], including Ir [26]. Ethylene glycol is both the reaction medium and the reduction agent. Metal salts, like ruthenium chloride and dihydrogen hexachloroiridate are used as noble metal precursors. For many catalysts a capping agent is required to stabilize the nanoparticles, but Bonet et al. [26] showed that EG on its own has enough of a stabilizing effect on the particles to avoid agglomeration, and a capping agent is not needed.

The reaction mechanism for oxidation of ethylene glycol has been elaborated by Bock et al. [27], as seen in . In this case a PtRu catalyst is synthesized from platinum and ruthenium chlorides, but the same oxidation reaction is here assumed to take place in the reduction of Ir from dihydrogen hexachloroiridate. The reaction takes place at elevated temperatures (>160°C, dependent on the noble metal), close to the boiling point of EG.
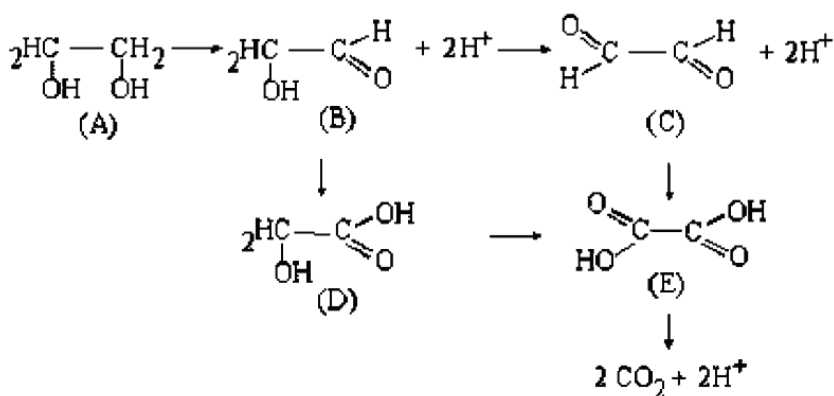

Figure 2.12: Oxidation pathway of ethylene glycol [27]. The alcohol (A) is reduced to aldehydes (B and C), which are further oxidized to glycolic acid (D) and oxalic acid (E). These may be oxidized further to CO_2 or carbonate.

The OH groups of the ethylene glycol react with the noble metal ions in the solution. The alcohol is reduced to aldehydes, which are unstable and oxidizes further to glycolic and oxalic acid. In alkaline media these may be further oxidized to CO_2 or carbonate.

In the same study [27], a correlation between the average particle size and size distribution, and the initial pH of the synthesis, controlled by addition of NaOH, was found. As shown in Table 2.1, the particle size decreases with increasing addition of NaOH, and thus increasing pH. The pH is decreased by a factor of 4-5 during the reaction.

Table 2.1: Influence of the NaOH Concentration on the Resulting PtRu Particle Size,
as reported by Bock et al. [27]

CNaOH [mol/L]	Initial pH	Final pH	PtRu particle size [nm]
0.1	11.1	6	0.7±0.5
0.085	10.5	5.5	1.2±0.5
0.075	10	5	1.5±0.8
0.071	9.5	4.5	2.0±0.8
0.069	7.8	4	2.2±0.8
0.068	7.5	3.5	3.0±1.5
0.063	7.2	3.3	4.0±1.5

The glycolic acid is present in its protonated form, HA, in acidic solutions, and in its deprotonated form, A^-, in alkaline solutions. The deprotonated form, called glycolate, is found to be a good stabilizer for the catalyst particles. Glycolate is a surfactant, binding itself to the particle surface, creating a colloid. The colloids repel each other, and will thus decrease agglomeration and particle growth. The concentrations of glycolate and glycolic acid are shown in Figure 2.13. At pH values above 6, the acid is present in its deprotonated form. This is consistent with the particle sizes in Table 2.1, where the smallest particle size is obtained with an end pH of 6, while for lower pH-values the syntheses yield larger particles. Solution pH values higher than 6 were found not to have any further effect on the particle sizes.
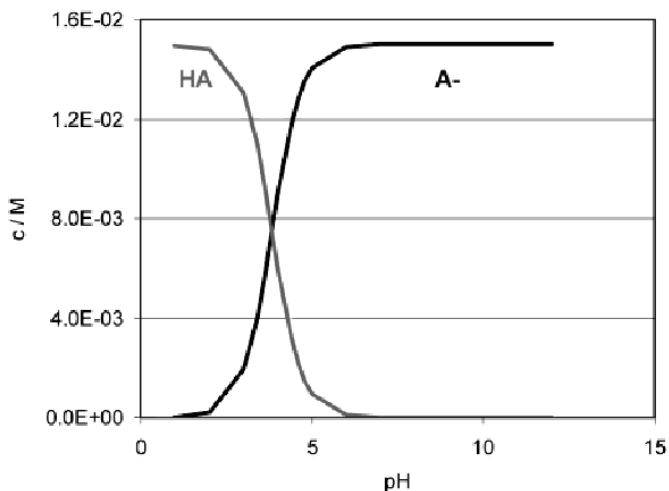
Figure 2.13: Dependence of the concentrations of glycolic acid (HA) and glycolate (A-) on the solution pH [27].

After the nanocrystals have been created, they must be deposited on the support particles. This is done by reducing the pH of the solution. This serves not only to remove the glycolate stabilizing the nanocrystals, as seen above, but will also alter the surface charges of the particles. This is due to the point of zero charge (pzc) [8] of the particles. When the pH of the solution is above the pzc of the material, the surface becomes negatively charged, while below the pzc the surface is positively charged. By tailoring the pH to a value between the points of zero charged for the noble metal and the support, the surfaces will be oppositely charged. The metal particles will then be attracted to the support surface by the electrostatic force, and will deposit evenly, as the equally charged particles will still repel each other.

Cacciuttolo [28] showed that reducing ruthenium from a ruthenium chloride precursor using the normal polyol method may yield lower loading values than expected. This may either be due to not all of the precursor material being reduced, or a loss due to reduced particles not depositing on the support. The first is a matter of the media temperature and time, and the latter is typically a matter of solution pH and electrostatic forces between catalyst and support. Samples of varying ruthenium content were found to have significantly less ruthenium than the target value. Ruthenium is less noble than iridium, meaning a greater EG temperature is needed to reduce ruthenium ions to ruthenium metal, than is the case for iridium, making ruthenium based oxides more difficult to synthesize with the normal polyol method.

2.6   Microwave polyol synthesis

Microwave-assisted reduction is a novel synthesis route for catalyst metal nanoparticles. Microwave irradiation gives rapid and uniform heating of the reaction medium up to reduction temperatures, and promises to significantly decrease the production time of supported catalysts in the lab. While the reaction and support assembly steps in the normal polyol method are

performed in the course of 24 hours, these steps may be done in the matter of minutes using microwave irradiation[29-35].

Though not all of the effects, both thermal and non-thermal, of the microwave irradiation are known, Anumol et al. [29] have done extensive work in evaluating the effects of heterogeneous nucleation - reduction of metal precursors in the presence of a substrate. If the dielectric loss in the substrate is greater than that of the reaction medium, the substrate will obtain a higher temperature than the medium. Using Pt/oxide in EG as their system, they hypothesized that this effect could cause selective formation of the metal onto the substrate. This is done by controlling the substrate temperature to be higher than the temperature needed for heterogeneous nucleation, while having the EG temperature be below the temperature needed for homogenous nucleation. Anumol et al. reduced Pt in presence of different oxide supports: CeO_2, TiO_2, ZnO and SiO_2. In all but the last case, they reported Pt nanoparticles forming on the substrate. In the case of SiO_2, the dielectric loss is lower than that of EG, so the metal is reduced homogenously in the medium, rather than on the substrate. This was further confirmed by reduction of Au in presence of other oxides. Table 2.2 summarizes the oxides studied, their dielectric properties and whether heterogeneous nucleation was observed.

Table 2.2: Oxides, dielectric properties, and nucleation results, as reported by Anumol et al. [29].

Material	Dielectric constant	Loss tangent	Heterogeneous nucleation
Al_2O_3	11,6 / 9,4	0,00005 / 0,00007	No
SiO_2	3,4	0,00016	No
MgO	9	0.007	Yes
TiO_2	50	0.002	Yes
CeO_2	23	0,001	Yes
ZnO	8,3	0,2	Yes

It is clear that the dielectric loss tangent is an important factor in heterogeneous nucleation. It should be noted that the loss tangent is dependent on the frequency of the irradiation. The dielectric properties of ethylene glycol and the ATO support will not be determined in this study, but the results of running the synthesis at different effects may provide a qualitative indication.

The microwave used by Anumol et al. is a scientific oven with high controllability in terms of temperature. Other studies (Lebegue et al., Harish et al.) [30-33] have successfully produced Pt and Ru catalysts on a carbon support with microwave pulsing in an advanced microwave. The advantage of using these ovens is great temperature control; the effect is kept continuous until a certain temperature is reached, then pulsed to keep the temperature steady.

Two other studies (X. Li et al. [34], Patel et al. [35]) reports creating a Pt/CNT catalyst by irradiation for 30s and 60s, and achieving homogenous nucleation of Pt and Pd catalysts, both in a standard household microwave. This study also reports that the synthesis pH is important for controlling the Pt particle size, with the particle size decreasing with the pH, from 5.8nm at pH 3.6, and 2.7nm at pH 9.2.

2.6.1   Ir/ATO catalyst synthesis

The preliminary project to this work established the microwave polyol synthesis as a successful method for creating ATO supported iridium oxide [4]. A standard household microwave was used in this project. Catalysts produced by this method proved to be working well, with catalytic activities close to the activity of catalysts produced by the normal polyol method. The normalized Tafel plots for these catalysts are shown in Figure 2.14. These show very similar activities between the different microwave synthesized samples, and also between the microwave samples and the control sample, EF003, produced by the traditional method.
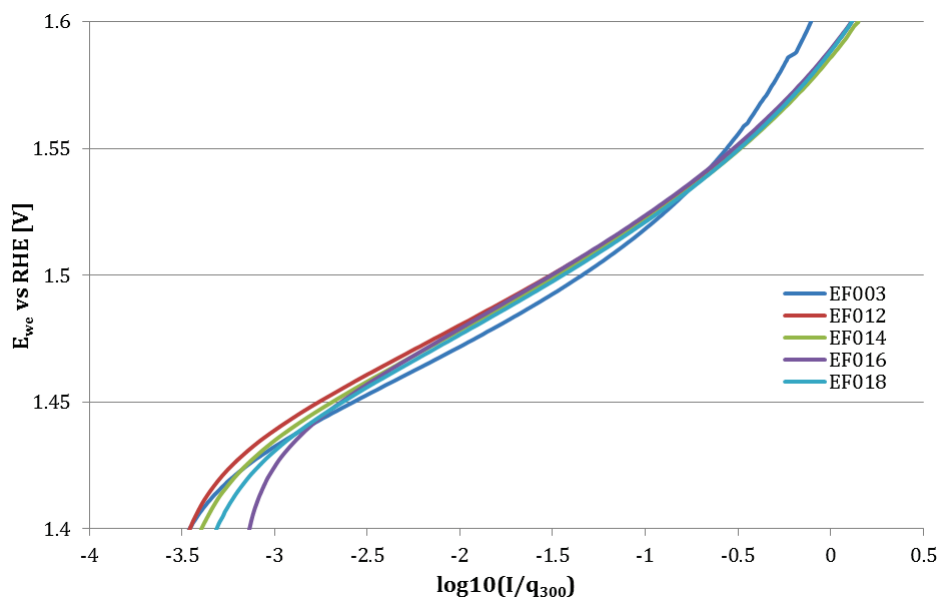

Figure 2.14: Tafel plots of linear sweeps recorded at 0.084 mV/s. The potential at the working electrode as a function of the logarithm of the normalized current. EF003 is the control sample, and the rest were produced by the microwave polyol method at varying synthesis conditions. [4]

The microwave synthesis was found to be a very time effective synthesis method, reducing the time required for the reduction and deposition steps from half a day to 6 minutes, and also removing several time-consuming steps such as heating and cooling the solution. In addition to this the microwave synthesis adds the ability to produce several unique catalyst batches simultaneously, rather than having to wait for one batch to be done before starting another. In the same time period required to produce one batch by the traditional method, 3 days including all steps, 8 unique batches were produced by the microwave method.

A parameter study was performed to investigate the effect of different synthesis conditions by changing the solution pH, heating power and heating time. Heating power was found to be clearly the most important of these parameters. 270 W power heating gave high enough temperature to achieve complete reduction of the precursor, while 90 W power did not create high enough temperature, yielding no iridium metal. Varying the solution pH did not yield any observable differences in the catalytic properties.

In addition to achieving target loading of iridium, the synthesis was found to yield a clear, colorless EG supernatant. This is an indication that there was no unreduced iridium left in the supernatant, and also that no iridium particles were stable in the solution instead of depositing on the support. At this point the microwave synthesis is advantageous over the traditional method, which from several trials yielded marginally transparent blackened EG at best, indicating not all the catalyst particles deposit on the support surface.

Another synthesis observation from the study was a sharp decrease in pH during the synthesis, with the pH decreasing from 10.5 at the start of heating, to around 1 after cooling the solution. This effect does not occur for the normal polyol synthesis. No explanation for this phenomenon was found during the study.

The study found large temperature variations in the reaction solution directly after heating. Internal temperature variations of up to 20 °C were found, with the higher temperatures at the surface and near the beaker walls. This correlates with the way dielectric heating works, with decreasing irradiation power as the microwaves are absorbed by the outer molecules. Natural convection is not strong enough to combat this effect, and forced convection is hard to perform in a standard microwave. This may be important to consider, as lower temperature zones within the solution may reduce the yield, especially when ruthenium is involved. Ruthenium, as discussed above, requires higher EG temperature to be reduced than iridium does.
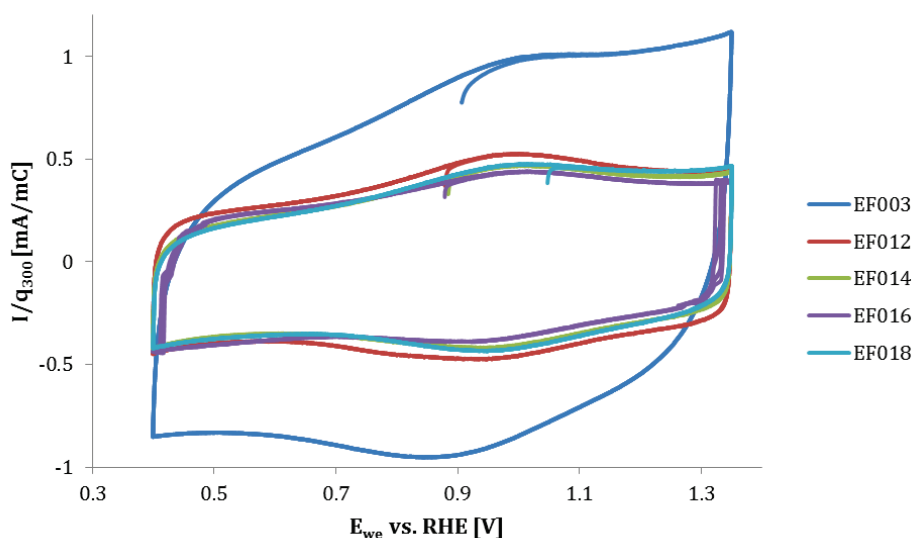
Figure 2.15: Non-normalized cyclic voltammograms recorded at 300 mV/s. EF003 is the control sample, while the rest are produced by microwave polyol synthesis.

The cyclic voltammograms produced from the microwave samples were found to be around half the size of the voltammograms from the control sample, as can be seen in Figure 2.15. Note that the areas of these curves provide some measurement of the catalyst surface areas of the samples, as will be discussed below. The cause of this difference was not thoroughly decided, but one major factor could be the preparation of the electrodes. The catalyst dispersions used to prepare the electrodes was very different in nature, with the dispersion of the control sample having larger visible particles which settled quickly, and the dispersions of the microwave sample being very stable with no visible particles. This influences how the catalyst deposits on the electrode surface, which again influences the catalyst surface available.

3 Experimental

3.1 Microwave polyol synthesis

The microwave polyol synthesis method, established in the preliminary work described in section 2.6.1, was used to produce powders of iridium, ruthenium and IrRu mixed catalyst, all supported on ATO. The equipment and chemicals used in the synthesis are listed in Table 3.1. A schematic of the method is seen in Figure 3.1.

Table 3.1: Equipment and chemicals used for the microwave synthesis

Chemicals	Equipment
Ethylene Glycol, anhydrous 99.8%, Sigma Aldrich	EM beakers, 300 ml
Dihydrogen hexachloroiridate(IV) hydrate, Alfa Aesar	Microwave, Kenwood KEN GJW25
	Dispersion tool, T25 Ultra-Turrax, IKA
Antimony tin oxide, ≳99.5%, Sigma Aldrich	Ultrasonic cleaner, VWR
	pH meter, Methrom
Nitrogen gas, AGA	Centrifuge, Biofuge primo, Heraeus

The ATO support was weighed out and dried overnight together with the glassware at 120 °C. The support was then dispersed in ethylene glycol and dispersed using a rotating dispersion tool. The support dispersion was added to the reaction beakers so that each beaker contained 450 mg of dispersed support. The metal precursors were then weighed out in a glove box, and consecutively dispersed in 5 ml ethylene glycol and added to the reaction beakers. The ruthenium precursor was found difficult to disperse properly in EG, so extra EG and an ultrasonic bath to make sure all of the precursor material would be added to the reaction beakers. The beakers were marked thoroughly with the synthesis number. Before heating, the pH of the solutions was increased to 11 using a few milliliters of 1M NaOH/EG solution. The solution was bubbled with nitrogen for 10 minutes, and then sonicated for 10 minutes before heating.

The microwave used was a standard household microwave, a Kenwood KEN GJW25. Output power is stated by the manufacturer as 900W, and the power settings are limited to 100%, 80%, 50% 30% and 10%. Operating frequency of the oven is 2450 Hz.
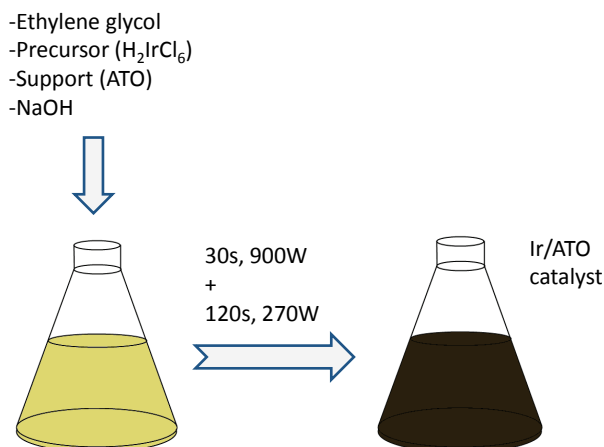
- Ethylene glycol
- Precursor (H_2IrCl_6)
- Support (ATO)
- NaOH

30s, 900W
+
120s, 270W

Ir/ATO catalyst

Figure 3.1: Schematic of the microwave-assisted polyol synthesis of an IrO_2/ATO catalyst.

The initial heating time at 100% power was increased from 30 seconds in the preliminary work to 40 seconds, to increase the solution temperature, and consequently the possibility of reducing the ruthenium precursor. Ruthenium is less noble and requires higher temperature than iridium to be reduced by ethylene glycol. The heating stage was followed by 6 minutes at 30%, during which the reaction media is expected to reach boiling temperature.

After the microwave heating, the temperature of the solution was measured, and the beakers were left to cool for a couple of hours. Once cool, the pH of the solutions was measured. The solution was then transferred to centrifuge tubes and centrifuged at 8400 rpm for 15 minutes to sediment the particles. The EG supernatant was decanted off, and its color noted. The particles were then redispersed in hot Mili-Q water, and then centrifuged again, and the water decanted off. This washing step was repeated three times, before the dispersions added to petri dishes, and dried overnight to yield dry catalyst powders. The dry powders were weighed to calculate the synthesis yield.

This synthesis method was used in this work to create the $Ir_{1-x}Ru_x$/ATO catalysts listed in Table 3.2. This includes one pure Ir/ATO sample and three pure Ru/ATO samples of varying catalyst loading.

Table 3.2: Microwave synthesized mixed oxide catalysts of
$Ir_{(1-x)}Ru_x$/ATO. Loading and compositional values are target values.

Synthesis number	Catalyst loading [wt%]	Ru in catalyst [at%]
EF020	20	0
EF021	20	5
EF022	20	10
EF023	20	20
EF024	20	100
EF025	25	100
EF026	30	100

3.1.1 Physical catalyst mixes

In addition to the atomically mixed catalysts listed above, three physical catalyst mixes was made to imitate the composition of samples EF021, EF022 and EF023. These were made by combining dispersions of EF020 and EF024 in ratios calculated from EDS measurements of the catalyst compositions.

3.2 Electrochemical analysis

The electrochemical analysis of the catalysts consists of several different voltammetry techniques performed on a gold rotating disc electrode covered with a thin film of the catalyst. The voltammetry in this work was performed in a 0.5 M H_2SO_4 electrolyte. A reversible hydrogen reference electrode (RHE) was prepared fresh for each analysis. Several techniques are built together for one analysis.

The potentiostat used was the VMP3 Multi Potentiostat from BioLogic, and the data was collected by the EC-lab software. The capturing software filters the current measurements over 10 data points. Further data processing, including numerical integration to calculate charges, current normalization, curve fitting and data plotting, was performed in MATLAB

Table 3.3: Equipment and chemicals used for electrochemical characterization.

Chemicals	Equipment
Sulfuric acid, 96%, Merck	Potentiostat, VMP3 Multi Potentiostat, BioLogic Science Instruments
Nafion, 5wt%, Alfa Aesar	RHE reference electrode
Argon gas, AGA	Platinum counter electrode
	Gold rotating disc electrode, Pine Research Instruments
	Rotating electrode speed control, Pine Research Instruments
	Ultrasonic cleaner, VWR
	Micropipettes

3.2.1   Electrode preparation

In order to analyze the catalyst by electrochemical methods, thin-film electrodes are prepared. For comparability, all electrodes are prepared in the exact same manner. A catalyst dispersion is prepared by weighing 6 mg of the catalyst in a glass container, and adding 3 ml Milli-Q water with pH 3. The catalyst is dispersed in an ultrasonic bath for at least 40 minutes, creating a uniform dispersion with a concentration of 2 mg/ml. This is done at least one day before the dispersion is deposited on an electrode, which is known to give a more stable dispersion. The uniformity of the dispersion is of high importance, in order to deposit the correct amount of catalyst.

Before the catalyst is deposited on the electrode, it is sonicated for 5 minutes to make the dispersion uniform. 20μl of the dispersion is deposited on a gold electrode using a micropipette and dried under argon, leaving 40μg of the catalyst on the electrode. When the electrode is dry, 10μl of 0.05wt% Nafion solution is added onto the electrode. The electrode is dried under argon and is ready to use.

The electrodes with the physical catalyst mixes mentioned in section 3.1.1 were prepared in order to mimic the exact amount of catalyst metal mass of iridium and ruthenium deposited. As there are slight variations in catalyst loading between the samples, the total deposited mass, including the support, was slightly different for these three samples.

3.2.2   Cyclic voltammetry

The lower and upper potential limits for the CV technique were 0.4 V and 1.35 V vs. RHE, respectively. The product from the synthesis is supported metal nanoparticles, which will oxidize only when a voltage is applied. The characterization is thus started with a 20-cycle sequence at

20 mV/s to fully oxidize the catalyst nanocrystals and form the metal oxide, then continuing with increasing sweep rate from 2 mV/s to 300 mV/s, as listed in Table 3.4.

Table 3.4: Cyclic voltammetry protocol. n_c is the number of cycles run for each sequence.

Sequence number	Sweep rate [mV/s]	n_c	Sequence number	Sweep rate [mV/s]	n_c
1	20	20	8	60	4
2	2	1	9	80	4
3	5	2	10	100	4
4	10	4	11	150	4
5	20	4	12	200	4
6	30	4	13	250	4
7	40	4	14	300	4

3.2.3   Linear sweep voltammetry

LSV measurements were performed directly after the cyclic voltammetry in the same cell setup. A rotation speed of 1800 rpm was applied to make sure oxygen gas bubbles would not form on the surface and block parts of the electrode area. The potential was swept from 1.3 V to 1.6 V vs. RHE with a sweep rate of 0.084 mV/s.

3.2.4   Accelerated stability testing

The AST degradation technique was performed directly after the first linear sweep. This technique consists of 10 000 cycles between 1.35 and 1.55 at a high sweep rate of 1 V/s, keeping the electrode rotation speed at 1800 rpm. Another linear sweep identical to the first was performed directly after the degradation cycle.

3.3   EDS

The chemical composition of the catalysts was determined by energy-dispersive x-ray spectroscopy (EDS) in a Hitachi S-3400N LVSEM. Samples were prepared on aluminum stubs from the dispersions prepared in section 3.2.1. The characteristic irradiation was recorded to 10 EDS spectra for each sample, and mass fractions were calculated by the AZtec software from Oxford Instruments. Due to problems detecting the correct oxygen mass fractions in the oxide support, the stoichiometry of ATO and the molar masses of Sn, Sb and O was used to calculate the weight fraction of the support. Due to the high interaction volume of the x-rays recorded by EDS, aluminum from the sample holder is recorded in the spectra. The catalyst loading was calculated for each spectrum by dividing the mass fraction of catalyst by the mass fraction of catalyst metal and support oxides. The average loading and standard deviation of the Ir loading was calculated for each sample.

3.4   TEM

Samples were imaged using a Jeol 2010F Field Emission Transition Electron microscope. The samples were prepared by dispersing a small amount of catalyst powder in ethanol using an ultrasonic bath. A small amount of the dispersion was then deposited on an amorphous carbon film supported by a copper grid. TEM operation and imaging was performed by Per Erik Vullum (SINTEF) in collaboration with the author. Particle sizes and size distributions were measured and calculated manually using ImageJ.

4 Results

4.1 TEM

The TEM imaging this work were performed on catalysts produced in the preliminary work, with the intention of comparing the morphology of microwave synthesized catalysts to the ones produced by the normal polyol method. This is in order to confirm that the microwave synthesis is a successful alternative to the normal polyol method. Images at two different magnifications, 60k X and 250k X, are shown below. EF003 is a catalyst produced by the traditional method, while EF018 is a catalyst produced by the microwave synthesis. Synthesis conditions for this work are based on the same parameters as EF018, so the morphology of this sample is assumed to be valid for the iridium based catalysts here.
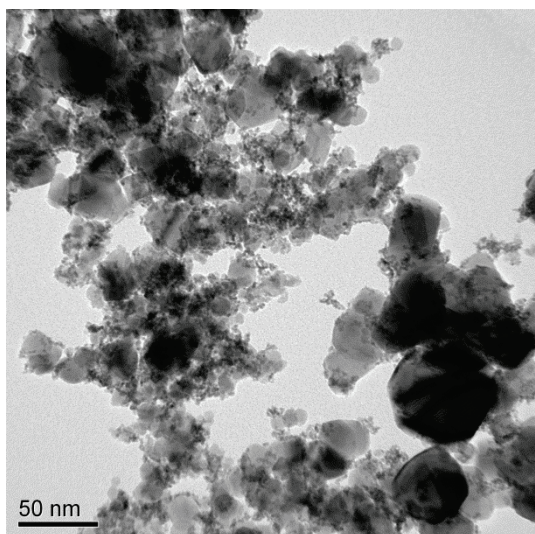
Figure 4.1: TEM image of EF003 at 60k X magnification
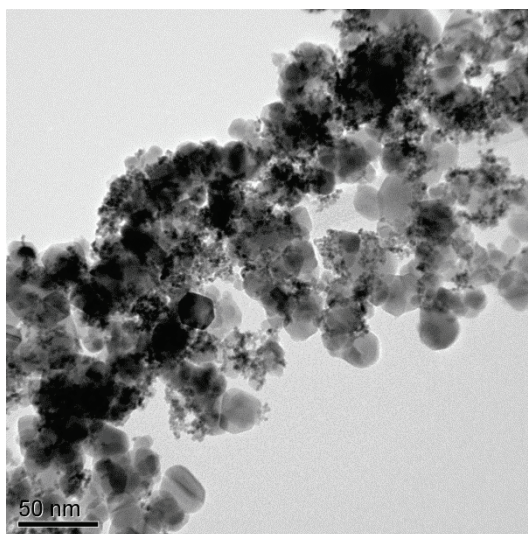
Figure 4.2: TEM image of EF018 at 60X magnification
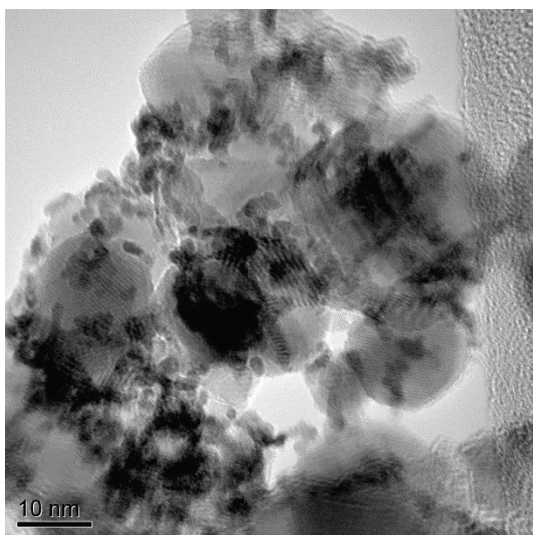
Figure 4.3: TEM image of EF003 at 250k X magnification
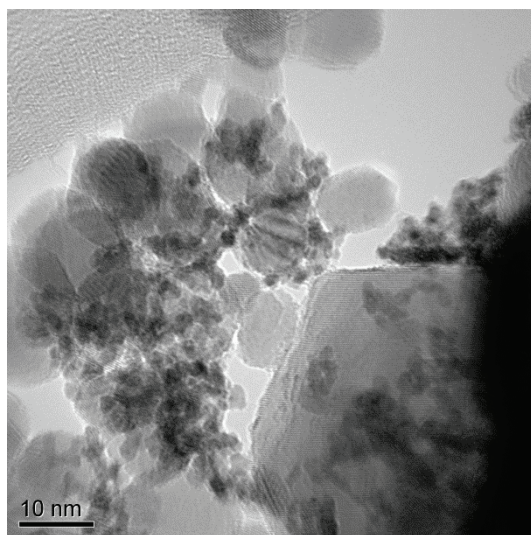
Figure 4.4: TEM image of EF018 at 250X magnification

The large particles seen in the images above are the support particles; while the smaller particles are catalyst metal itself. It can be seen that for both samples the catalyst particles are somewhat evenly distributed. There are some support areas without catalyst loading, especially in the microwave sample. In both cases there seem to be a degree of agglomeration of the catalyst particles, but this is not very excessive. Otherwise, there are no major differences between the morphologies of the samples.
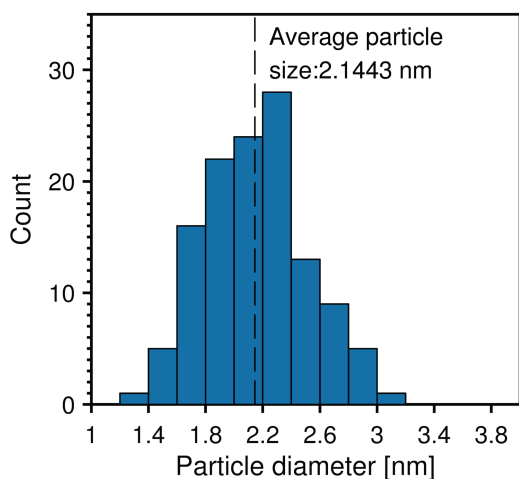
Figure 4.5: Size distribution of Ir particles in EF003
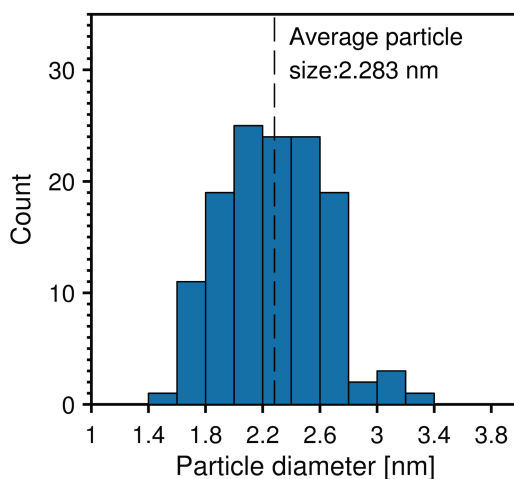
Figure 4.6: Size distribution of Ir particles in EF018

Figure 4.5 and Figure 4.6 show the size distribution of the catalyst particles, measured over several TEM images at 250X magnification. Both have an average particle diameter just above 2 nm and a size range from 1 to just above 3 nm.

4.2 Synthesis

Seven different batches of catalyst were produced by the microwave polyol method in this work, following the procedure presented in section 3.1. All catalysts are supported on ATO. The microwave polyol synthesis allows for several catalysts to be produced in parallel, so everything was produced in two separate runs. The first run handled the mixed oxide catalysts EF020-EF023, while the second produced ruthenium catalysts. Table 4.1 lists the maximum and measured synthesis yields. The yields for the first run were all above 80%, which is a high yield for a setup of this size. The yields for the second run were just above 50%, which is rather low. The source of the high losses is not clear from synthesis observations, though the washing and collecting steps are known to cause a certain loss.

Table 4.1: Synthesis yields

Synthesis number	Yield		
	Target [mg]	Measured [mg]	Percentage
EF020	562.5	447.4	80%
EF021	562.5	473.3	84%
EF022	562.5	487.2	87%
EF023	562.5	483.1	86%
EF024	562.5	271.5	52%
EF025	600.0	346.5	58%
EF026	642.9	370.8	50%

During the first run there were some difficulties in dissolving all of the precursor powder in EG before adding to the reaction vessel. The problem was believed to be related to the $RuCl_3$ precursor, as the amount of undissolved precursor increased with increasing target ruthenium composition. This was confirmed in the second run, where $RuCl_3$ was the only precursor, and there were major difficulties in dissolving all of it. This was solved by using more EG and an ultrasonic bath to dissolve and add the precursor to the reaction vessel in steps. This led to some more solution volume than planned in the first run, and significantly more (~15 ml) in the second run.

Table 4.2 lists the pH and temperature measurements performed before and after the reaction step of the synthesis. The end pH was measured after letting the solution cool down to room temperature. The steep pH drop during the reaction of the same magnitude as observed in the preliminary project.

Table 4.2: Measured initial pH, end pH, and end temperature of the synthesis solutions

Synthesis number	Initial pH	End pH	End temperature [°C]
EF020	11.0	1.4	184
EF021	11.0	1.5	185
EF022	11.0	1.5	183
EF023	11.0	1.5	186
EF024	11.0	1.5	-
EF025	11.0	0.9	-
EF026	11.0	0.9	-

During the first run, the reaction solution reached the boiling point of EG for all the samples. Boiling was observed and some vapor was expelled through the microwave vent. During the second run, boiling was not observed. This may well be because of the increased solution volume mentioned above. Unfortunately, the end temperature was not measured for this run.

For all syntheses, both the EG and water supernatant form the washing steps was clear and mostly colorless. A very slight green tint in the EG supernatant was observed for the ruthenium syntheses, especially EF026.

4.2.1   *Effect of microwave heating on the pH*

In order to investigate the pH drop observed in the microwave synthesis, an experiment was conducted using EG and ATO without any precursor. One vessel with pure EG and one vessel with 450 mg ATO dispersed in EG was treated to the same heating as during synthesis. The pH was adjusted using a 1M NaOH/EG solution prior to heating. Table 4.3 shows the measured pH and temperatures from the experiment.

Table 4.3: Measured initial pH, end pH, and end temperature of the solutions

Solution	Initial pH	End pH	End temperature [°C]
75 ml pure EG	9.86	9.5	187
75 ml EG + 450 mg ATO	9.83	1.5	187

No significant change in pH is present for the pure EG solution, while for the EG/ATO solution the drop is of the same magnitude as during synthesis, indicating there is some reaction happening when ATO is present during heating, and that this happens without reduction of a metal precursor.

4.3   EDS

EDS measurements were used to find the chemical composition of the samples, in order to calculate both the catalyst metal loading and the composition of the catalyst metal. As the oxygen

content is not detected accurately by EDS, the support mass fraction was calculated from the stoichiometry of the oxides, SnO_2 and Sb_2O_5. Calculations are based on 12 point and area measurements from one site per sample. The composition was calculated for each measurement, and then the average values and standard deviations were calculated from those. The EDS results are listed in Table 4.4.

Table 4.4: EDS measurements of catalyst loading and composition

Synthesis number	Catalyst loading [wt%]			Ru in catalyst [at%]		
	Target	Measured	Standard deviation	Target	Measured	Standard deviation
EF020	20	21.13	1.59	0	0	-
EF021	20	21.72	1.18	5	4.74	1.34
EF022	20	21.59	1.30	10	6.70	1.55
EF023	20	21.33	0.67	20	14.13	1.38
EF024	20	22.19	2.96	100	100	-
EF025	25	26.73	1.67	100	100	-
EF026	30	28.70	2.08	100	100	-

The catalyst loading is very close to the target for all samples and higher than target for most of them. Note that the standard deviations are relatively high. For the mixed oxide catalysts, the ruthenium content is somewhat lower than the target value.

The EDS measurements of EF021, EF022 and EF023, the mixed oxide catalysts, was used to create physically mixed catalysts of iridium and ruthenium. Samples EF027, EF028 and EF029 imitate the three above, respectively. When performing EDS to confirm the composition of these physically mixed catalysts, the software was unable to correctly detect and quantify the ruthenium content.

Table 4.5: List of physical catalyst mixes created from pure Ir/ATO and Ru/ATO

Synthesis number	Note	Target ruthenium content [at%]
EF027	Imitation of EF021	4.74
EF028	Imitation of EF022	6.70
EF029	Imitation of EF023	14.13

4.4 Electrochemical characterization

4.4.1 Cyclic voltammetry

Figure 4.7 shows a comparison of the voltammograms for Ir/ATO and Ru/ATO. The current values are normalized by the charge at 300 mV/s, q_{300}. The voltammogram shapes of the two samples are very distinct. Iridium oxide has an anodic (positive) peak at 1.02V, while ruthenium oxide has an anodic peak at 0.75 V.
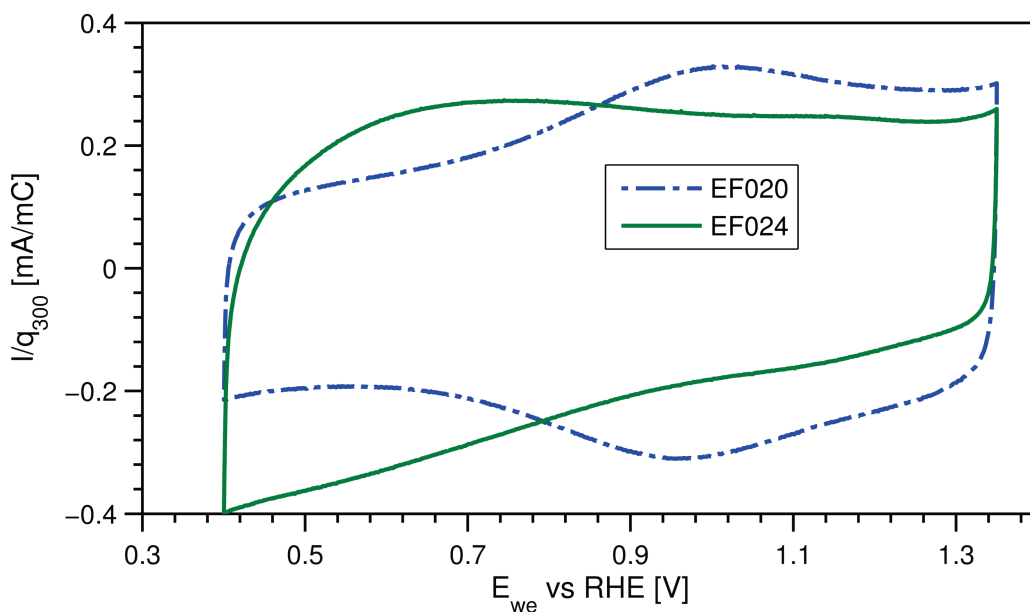
Figure 4.7: Normalized voltammogram of pure iridium and ruthenium oxides. Anodic peaks are seen around 1.02 V and 0.75 V, respectively.

Figure 4.8 shows how the voltammogram evolves during the oxidation cycling. It can be seen that the area of the curve increases during the cycling, as the anodic peak becomes larger and shifts towards the right.
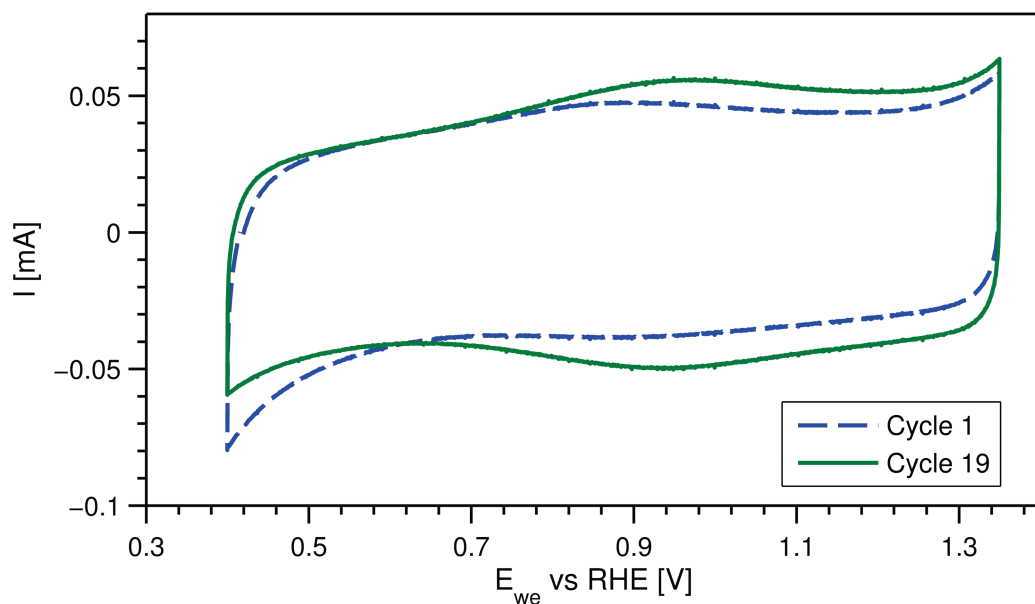
Figure 4.8: The development of the voltammogram during the oxidation cycling at the start of the voltammetry protocol. Sample EF022 (6.7 at% Ru).
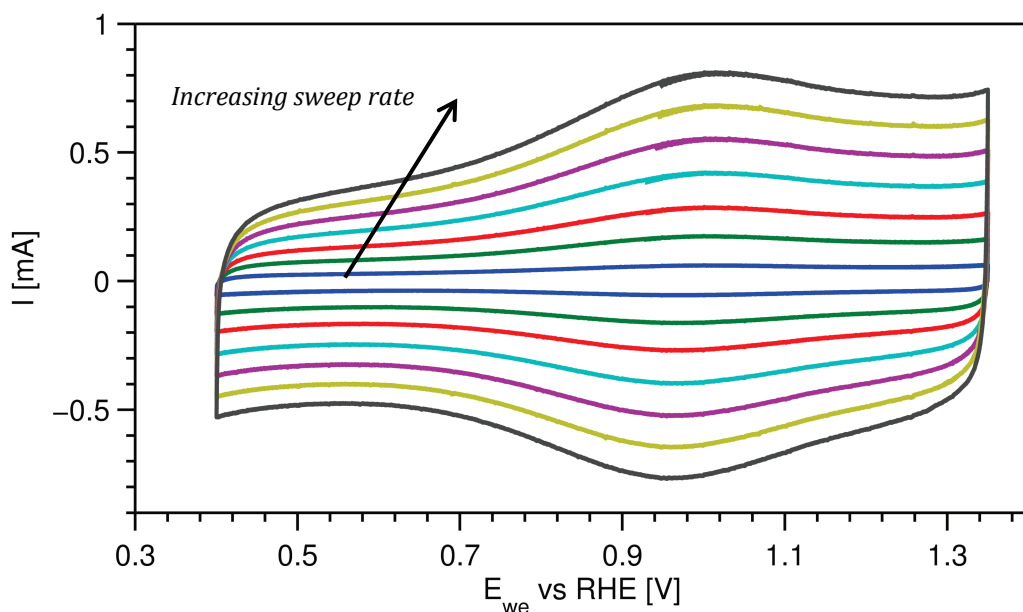
Figure 4.9: Voltammograms for EF020 at increasing sweep rate. The inner cycle is for 20 mV/s, and the outer is for 300mV/s.

Figure 4.9 shows the behavior of the voltammograms for EF020 for increasing sweep rates. The anodic peak potential is hard to distinguish, especially for the lower sweep rates, but numerical analysis shows that the potential does not change significantly as the sweep rate increases.

Figure 4.10 shows the normalized voltammograms of the pure oxide and atomically mixed oxide catalysts. The voltammogram shapes for the mixed oxides are very close to that of pure iridium oxide, which is to be expected as the iridium content is dominant in all samples. There is a slight shift of the anodic the peak from around 1.02 V for EF020 to 0.95 V for EF023, which is 14.7 at% ruthenium. It can be seen that the shapes get slightly more similar to that of pure ruthenium oxide, as the ruthenium content increases, with higher currents around the ruthenium oxide anodic peak at 0.75 V.
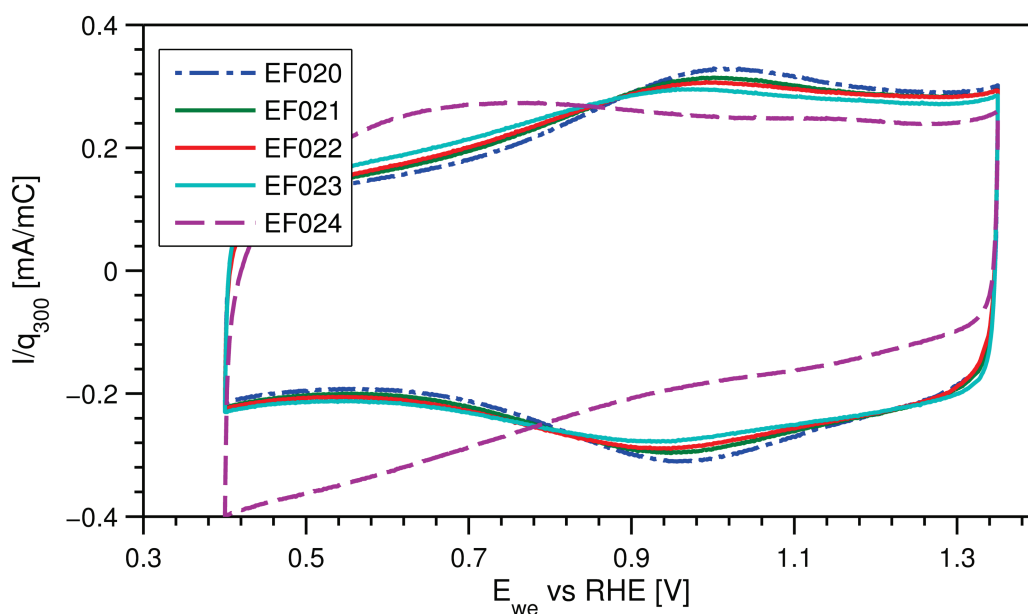
Figure 4.10: Normalized voltammogram of pure and atomically mixed oxide catalysts.

Figure 4.11 shows the normalized voltammograms for the mixed oxide samples, along with the pure iridium and ruthenium oxide samples. Curiously, the anodic current peak shift observed above does not appear here, even though the physically mixed samples imitate the composition of the atomically mixed samples.
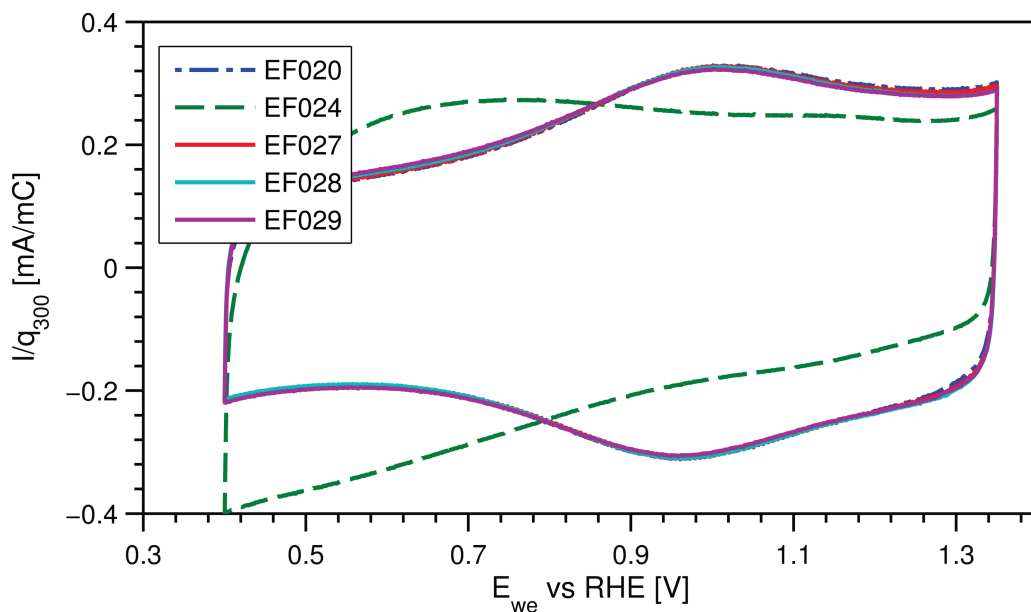
Figure 4.11: Normalized voltammograms for physically mixed oxides and pure oxide samples.

4.4.2   *Normalization of current*

The charge at 300 mV/s is calculated by numerical integration of the anodic current between 0.5 V and 1.3, as a function of time. Note that the voltammograms above are current as a function of voltage, not time. Table 4.6 lists the q_{300} for all samples tested in this work.

Table 4.6: Calculated charges at 300 mV/s for all samples

Synthesis number	q_{300} [mC]
EF020	2.47
EF021	2.39
EF022	2.59
EF023	2.75
EF024	1.31
EF027	2.23
EF028	2.08
EF029	2.20

Note that the charge is directly dependent on the total mass of the catalyst for particles of this size, and is thus strongly dependent on the electrode preparation. During this work there was some difficulty in preparing the electrodes, and the surface area may change between different electrodes with the same catalyst.

Charges for the other sweep rates have been calculated as well. Figure 4.12 and Figure 4.13 shows the relationship discussed in section 2.3.4, with the charge as a function of the inverse of the square root of the sweep rate, and the inverse of the charge as a function of the square root of the sweep rate, for the mixed oxide samples. Figure 4.14 and Figure 4.15 does the same for the pure oxide catalysts and the physical mixes.

As was the case for the preliminary work, there is no clear linear relationship as described in section 2.3.4, at least not clear enough to be able to extrapolate and calculate the total and outer charges
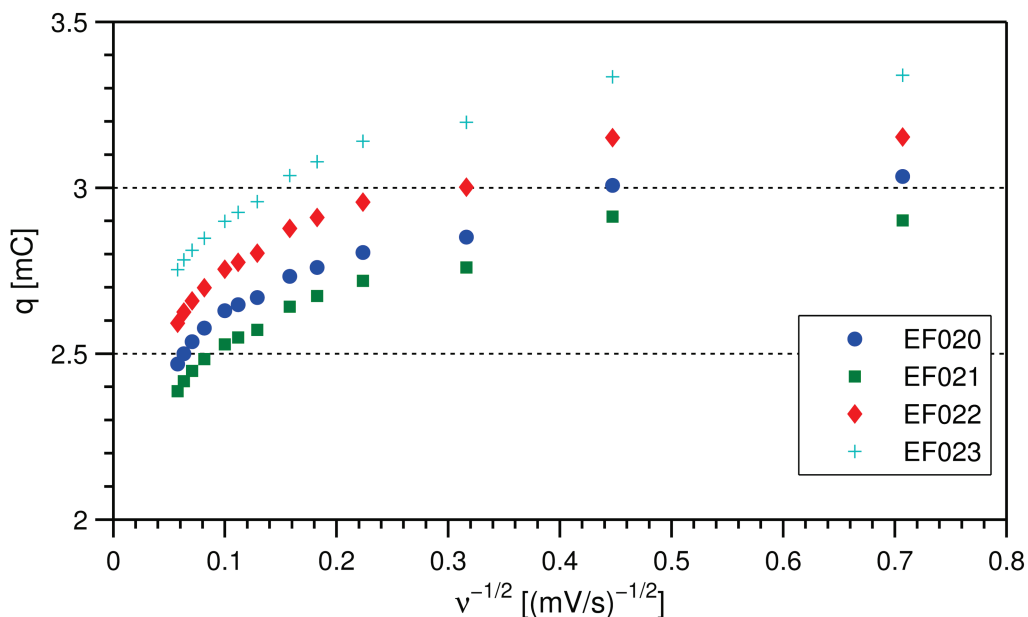
Figure 4.12: The charge as a function of the inverse of the square root of the sweep rate. Atomically mixed oxide catalysts.
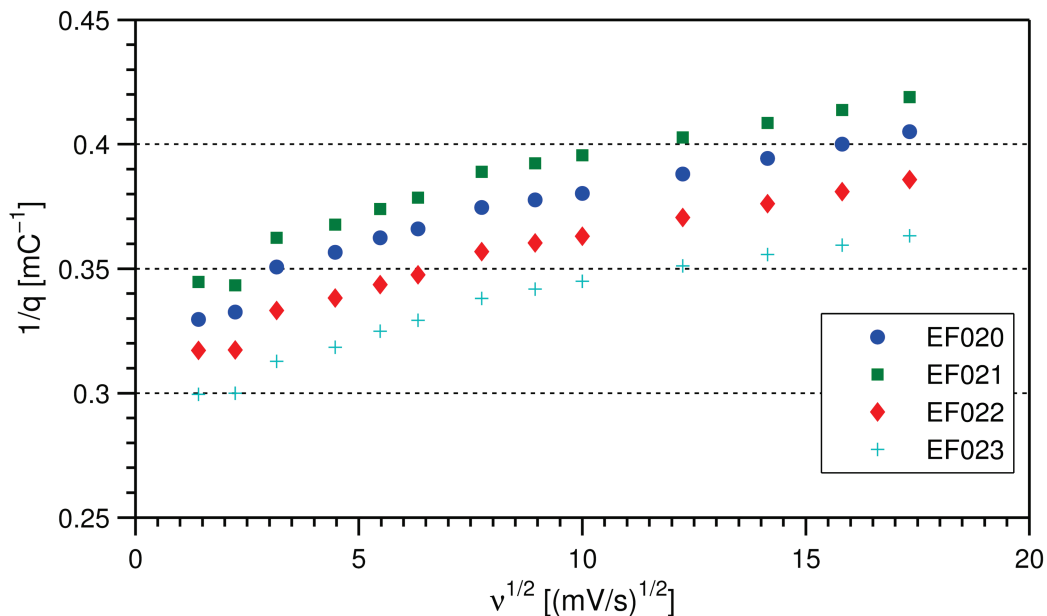
Figure 4.13: The inverse of the charge as a function of the square root of the sweep rate. Atomically mixed oxide catalysts.
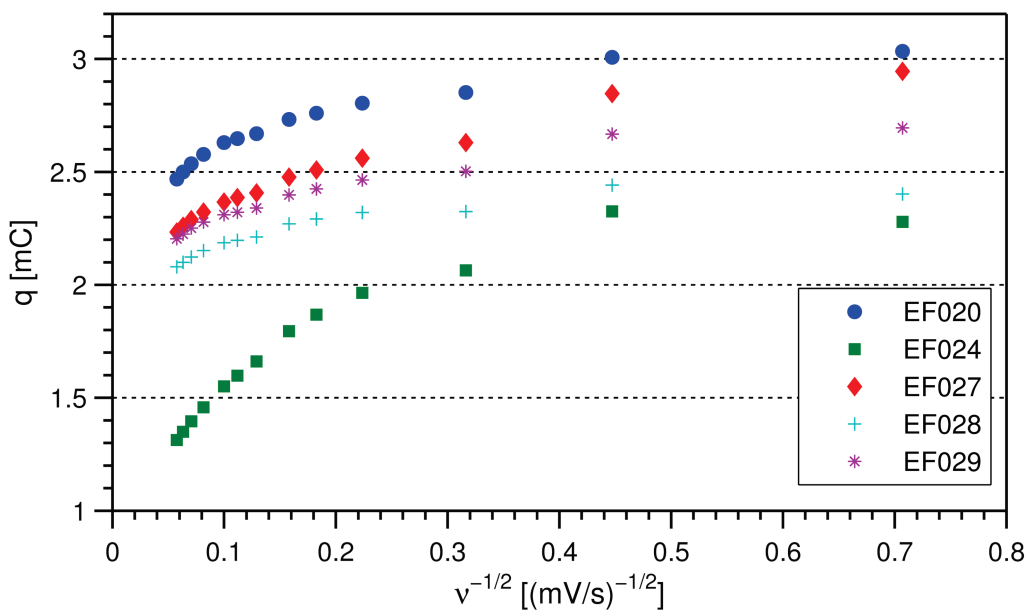

Figure 4.14: The charge as a function of the inverse of the square root of the sweep rate. Physically mixed and pure oxide catalysts.
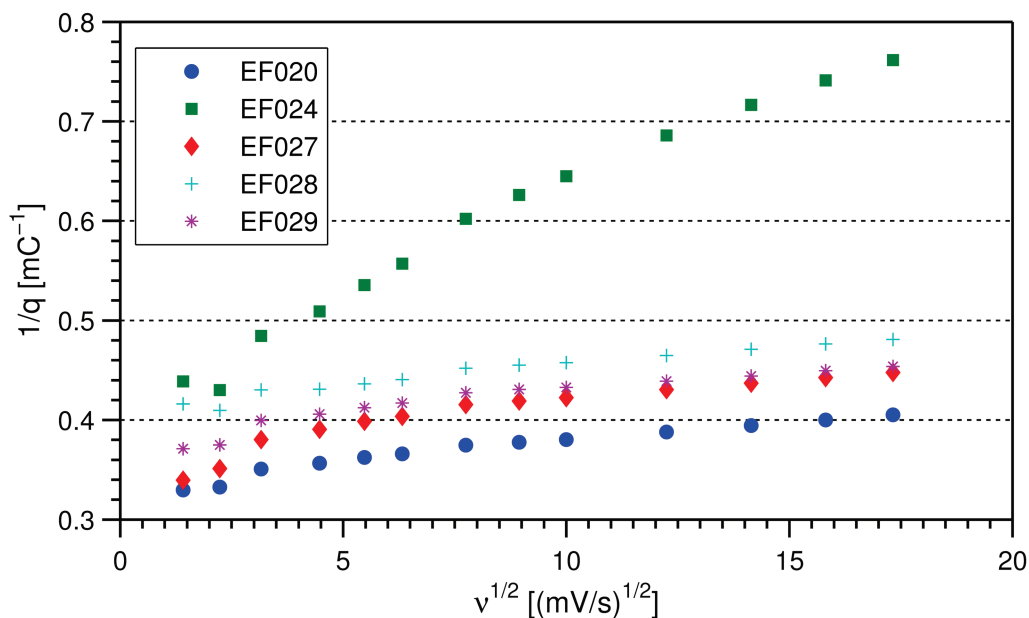
Figure 4.15: The inverse of the charge as a function of the square root of the sweep rate. Physically mixed and pure oxide catalysts.

4.4.3   Linear sweep

Figure 4.16 and Figure 4.18 show the normalized current-voltage plots for the mixed oxide catalysts, and the physically mixed and pure oxide catalysts, respectively. Note that EF024, the pure ruthenium oxide sample, shows an early current peak before the current decreases again. A small bump can also be seen for the physical mixes EF029 and EF028. For the pure iridium and atomically mixed oxide catalysts, the current only rises. It can be seen that the current increases as a function of ruthenium content for the atomically mixed oxides.

Figure 4.17 and Figure 4.19 are the Tafel plots for the same samples. The Tafel plots show how there is a linear region at low voltage, determined by the Tafel equation. At higher currents resistance in the cell causes the curve to bend upwards Figure 4.19 shows in detail the behavior of the samples containing ruthenium oxide particles at low current. The pure ruthenium oxide catalyst has a very high activity at low voltage, but bends upwards and backwards, towards lower current densities, around 1.45 V. The same bend appears around 1.46 V for the physical mixes, but these stabilize to have an activity just below that of the pure iridium oxide sample. The activity loss is known to be due to dissolution of the ruthenium particles due to the low stability of the oxide.
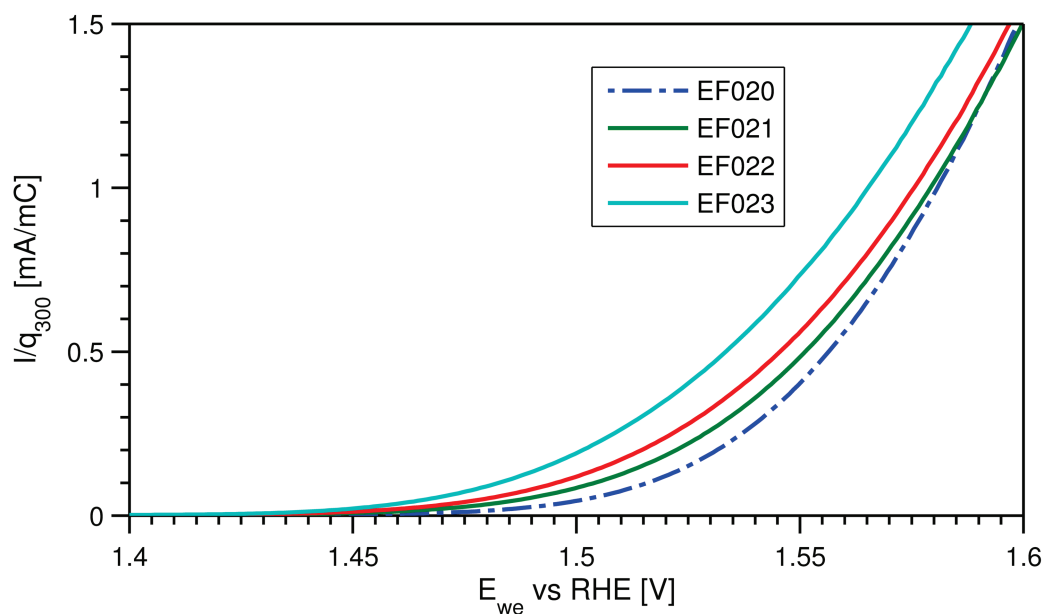
Figure 4.16: Normalized current-voltage plot from linear sweep at 0.084 mV/s. Atomically mixed oxides.
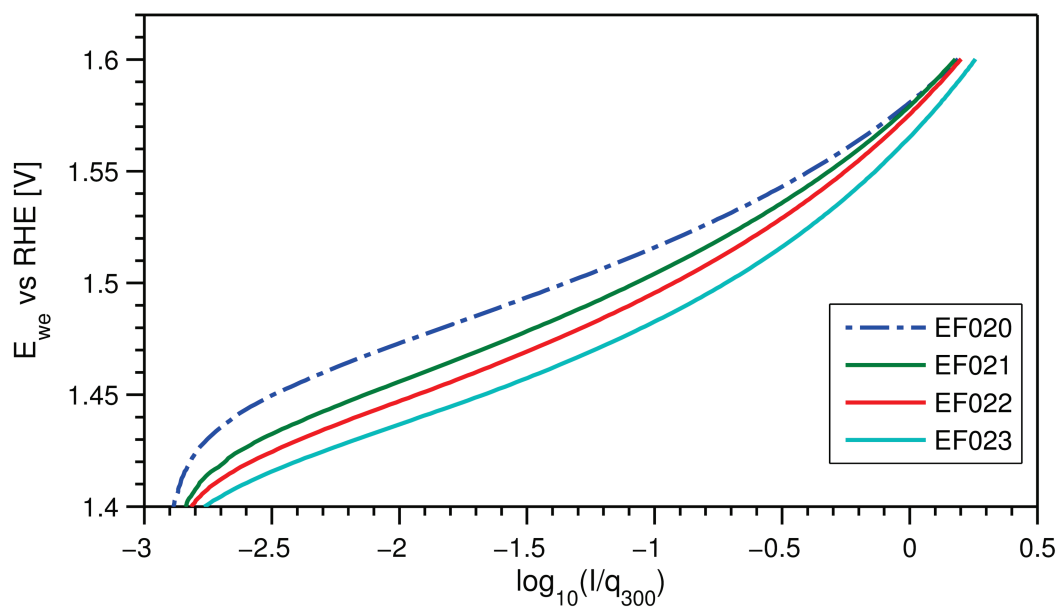

Figure 4.17: Tafel plot recorded at 0.084 mV/s. Atomically mixed oxides.
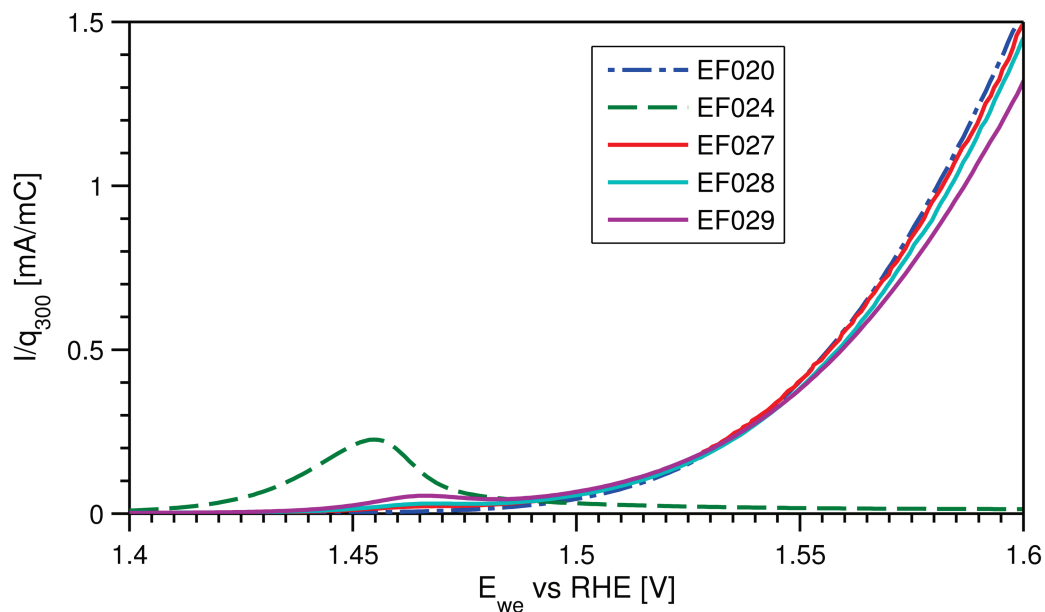
Figure 4.18: Normalized current-voltage plot from linear sweep at 0.084 mV/s. Physically mixed and pure oxides.
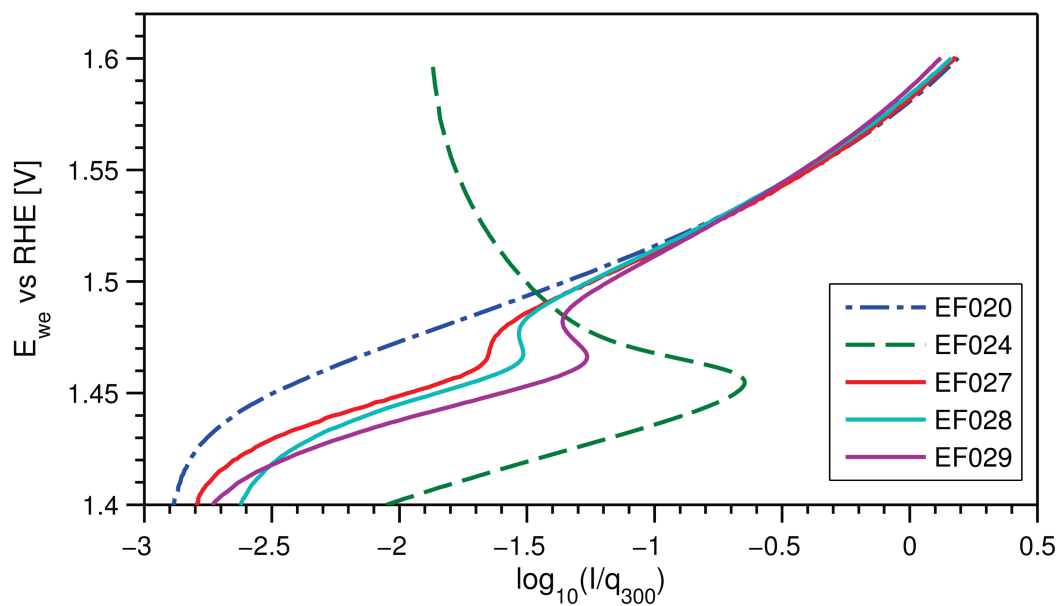

Figure 4.19: Tafel plot recorded at 0.084 mV/s. Physically mixed and pure oxides.

4.4.4   *Ohmic loss compensation*

Figure 4.20 shows how the constants *a* and *b* for the Tafel equation (2.11) may be found by fitting the terms of equation 2.13 to the experimental data, as discussed in theory in section 2.3.5.

$$\eta \; = \; a \; + \; b \log |i| + iR \qquad\qquad \text{(2.13 rep.)}$$

The equation has been fitted to the data within the dashed lines using the Levenberg–Marquardt algorithm. At higher currents bubble formation on the electrode surface provides an extra term to the equation, meaning fitting the equation to higher currents gives a visibly poorer fit for the linear region.

For the samples containing pure ruthenium oxide catalyst, the degradation of the catalyst around 1.45 V means fitting to equation (2.13) becomes harder. In order to find the best fitting results the range was limited to before the degradation. For the physical mixes, this led to the best fit being found by fitting the Tafel equation without the *iR* term, as otherwise the algorithm tended to find a very large R and a visibly incorrect approximation to the linear region. The pure ruthenium oxide sample reaches relatively high currents before degrading, so here the full formula was used for fitting.

Figure 4.21 shows the uncompensated ohmic loss for the same sample. This is calculated as the difference between the raw data and the linear Tafel equation, thus representing the *iR* term of equation (2.13). If the curve fitting is accurate, this plot should be linear with relation to the current density, and should, if extrapolated, intersect the origin. Figures showing the equation-fitting for the other Tafel plots may be found in appendix A.
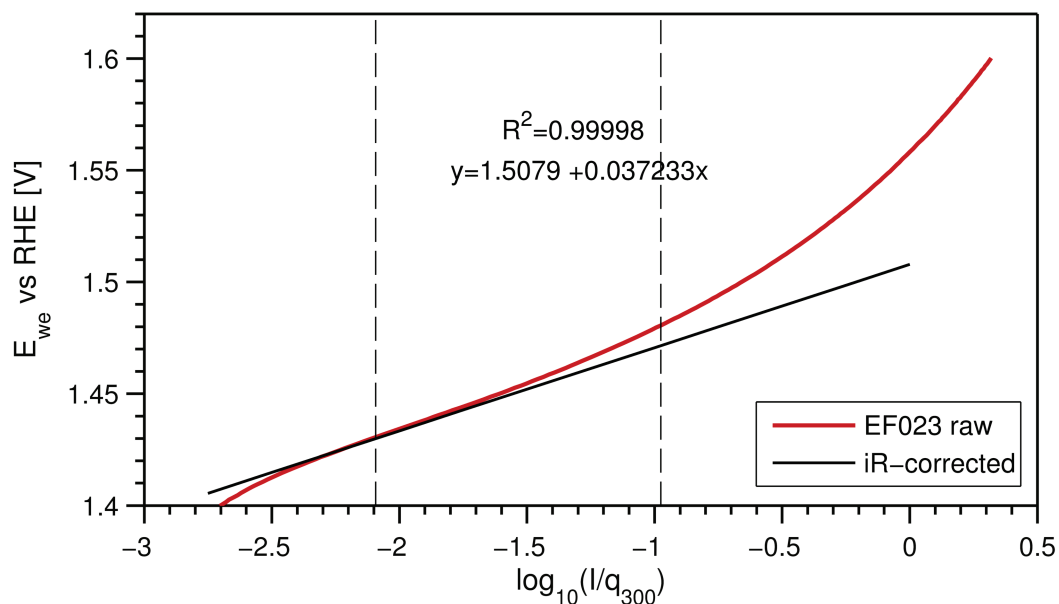
Figure 4.20: Approximation of the linear region in the Tafel plot of EF023. The data for the linear approximation are found by fitting equation (2.13) to the experimental data by the Levenberg Marquardt algorithm. The dashed lines mark the region where the fit was performed.
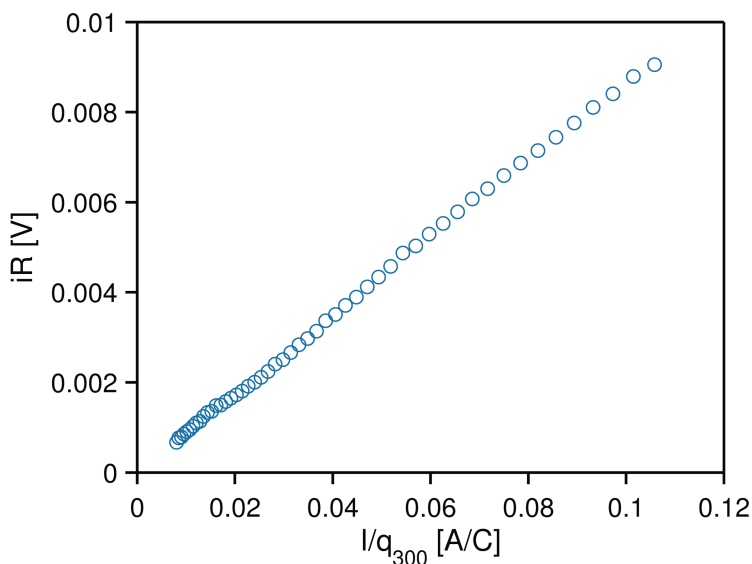

Figure 4.21: Uncompensated ohmic loss for EF023, calculated as the difference between the raw data and the linear approximation.

Table 4.7 lists the constants *a* and *b* found from the curve fitting for all samples. Figure 4.22 plots the Tafel slopes *b* as a function of the composition.

Table 4.7: Tafel constants

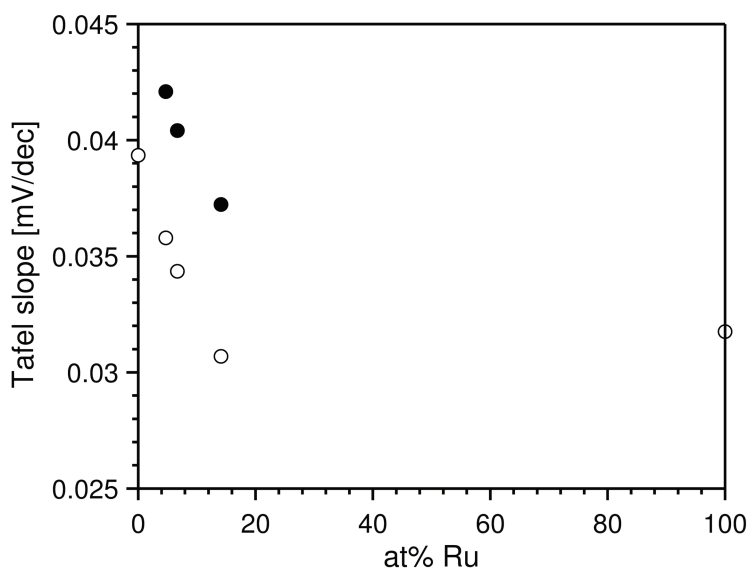| Synthesis number	*a* [V]	*b* [V/dec]
EF020	1.551	0.03935
EF021	1.540	0.04209
EF022	1.526	0.04041
EF023	1.508	0.03723
EF024	1.476	0.03175
EF027	1.523	0.03580
EF028	1.518	0.03435
EF029	1.502	0.03070

Figure 4.22: Tafel slopes found from curve fitting as a function of ruthenium content. Filled circles are atomic mixes and open circles are physical mixes and pure oxide catalysts.

With the fitting constants in hand, iR compensated normalized currents may be calculated by the Tafel equation, making it possible to compare the catalysts without the cell resistance. The figures below compare the activities of the catalysts as a function of the ruthenium content, as described in section 2.4, in order to compare it to the results of Kötz and Stucki[6] and Owe et al[5]. Note that compositions are for the whole particle volume as measured by EDS, and may not be accurately representing the surface concentration.

Figure 4.23 shows the iR corrected charge normalized current at a potential of 1.5 V, calculated by the fitting constants and the Tafel equation, as a function of the ruthenium content in the sample. The figure includes linear fits to the atomic and physical mixes.
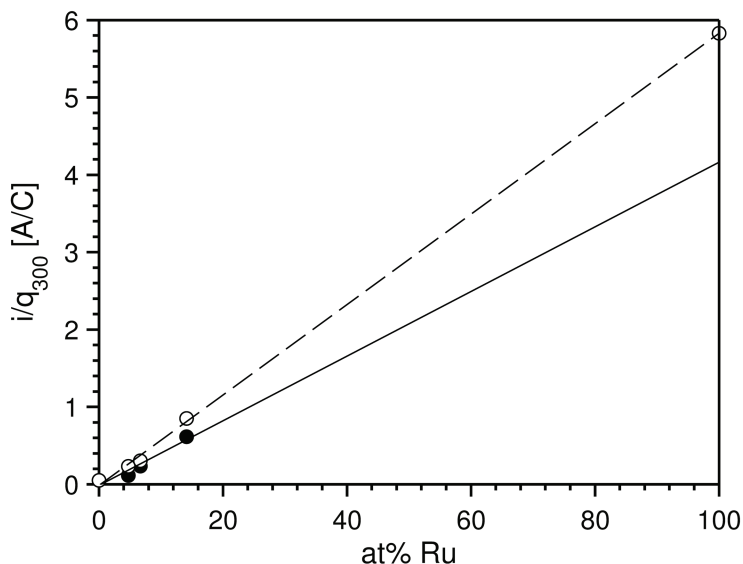
Figure 4.23: iR-corrected normalized current at 1.5 V as a function of the average ruthenium content of the catalyst metal. Filled circles are atomic mixes and open circles are physical mixes and pure oxide catalysts. The dashed line is the best fit linear function for the physical mixes and pure oxides, while the solid line is the fit for iridium oxide and atomic mixes.

Figure 4.24 shows how the potential at a normalized, iR compensated current of 10mA/C changes as a function of the ruthenium content. The dashed line linearly connects the pure oxide catalysts. This was the relationship found by Kötz and Stucki in their study f sputtered oxide films. The solid line shows the potential calculated as the sum of individual contributions from iridium and ruthenium oxides using equation (2.14), using the constants found from the curve fitting, listed in Table 4.7. The data seem to follow along the lower curve. Figure 4.25 and Figure 4.26 show the same for iR compensated normalized currents of 0.1 and 1 A/C.
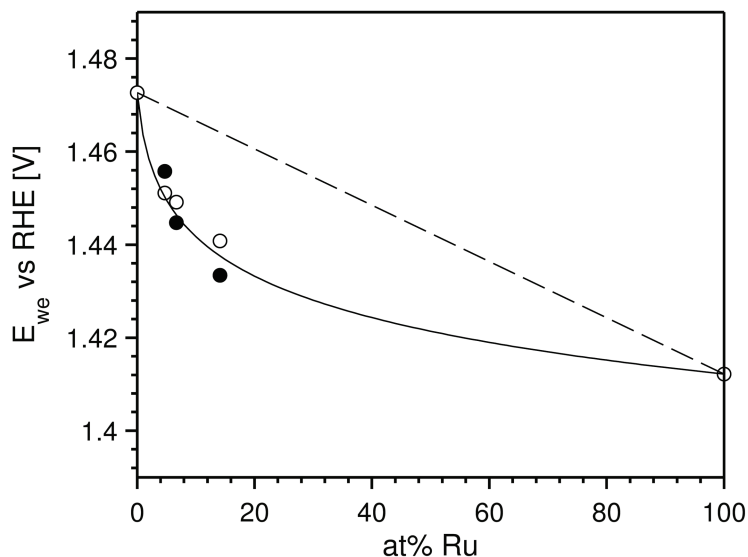
Figure 4.24: Potential required for an iR-corrected normalized current of 10 mA/C as a function of the ruthenium content of the catalyst metal. Filled circles are atomic mixes and open circles are physical mixes and pure oxide catalysts. The solid line is the potential calculated by assuming the total current is the sum of partial currents of the two oxides.

Figure 4.25: Potential required for an iR-corrected normalized current of 0.1 A/C as a function of the ruthenium content of the catalyst metal. Filled circles are atomic mixes and open circles are physical mixes and pure oxide catalysts. The solid line is the potential calculated by assuming the total current is the sum of partial currents of the two oxides.
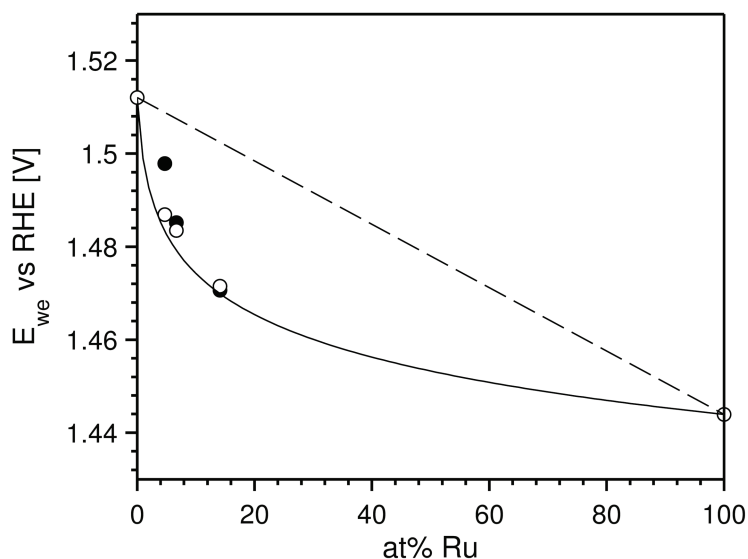
Figure 4.26: Potential required for an iR-corrected normalized current of 1 A/C as a function of the ruthenium content of the catalyst metal. Filled circles are atomic mixes and open circles are physical mixes and pure oxide catalysts. The solid line is the potential calculated by assuming the total current is the sum of partial currents of the two oxides.
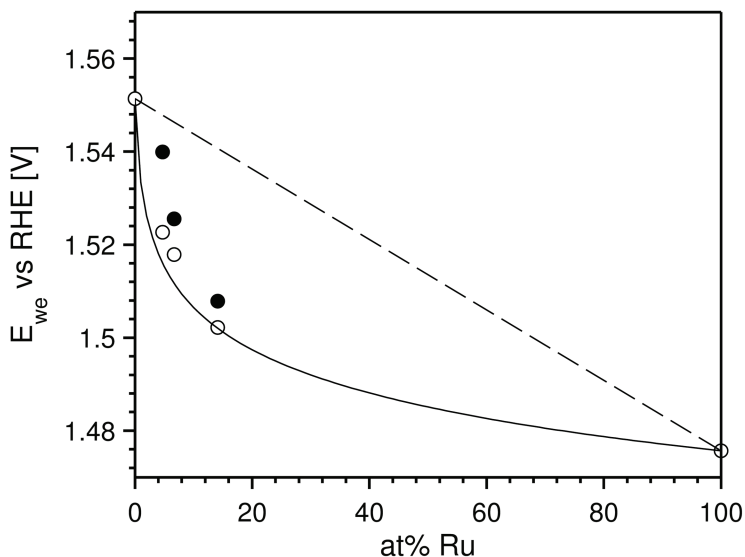
The figures below compares the real polarization curves of the physically mixed catalysts with calculated curves, which are calculated by adding weighted current contributions from ruthenium and iridium oxides at a given potential. It can be seen that the calculated Tafel plot bends off at lower currents and lower potentials than the real one.
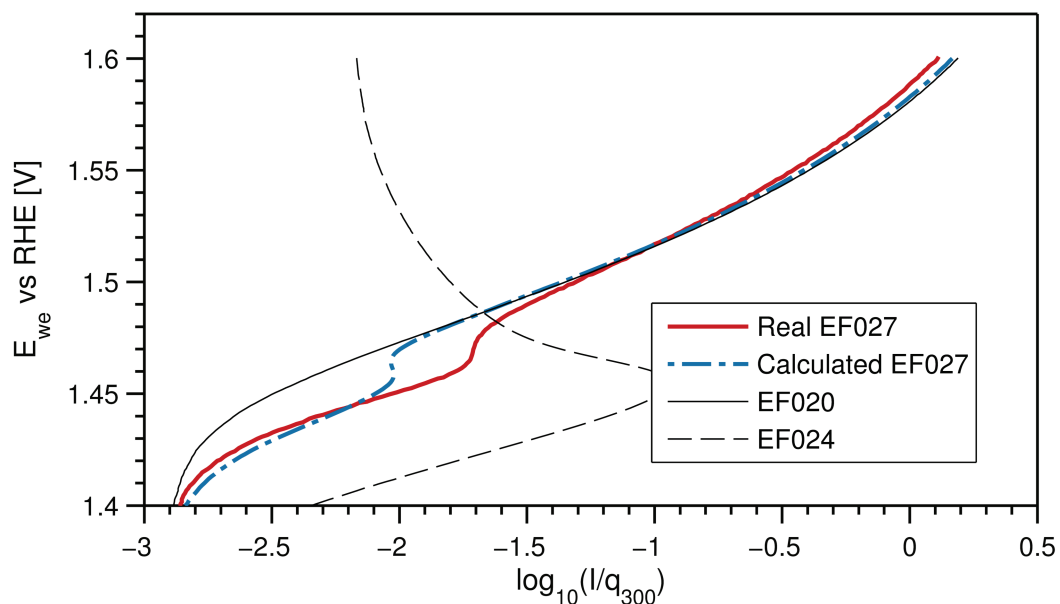
Figure 4.27: Comparison of real and calculated Tafel plots for EF027, the physically mixed catalyst with 4.7 at% ruthenium. Calculated plots are the sum of current contributions from ruthenium (thin dashed line) and iridium (thin solid line) oxides at a given potential, weighted by the composition.
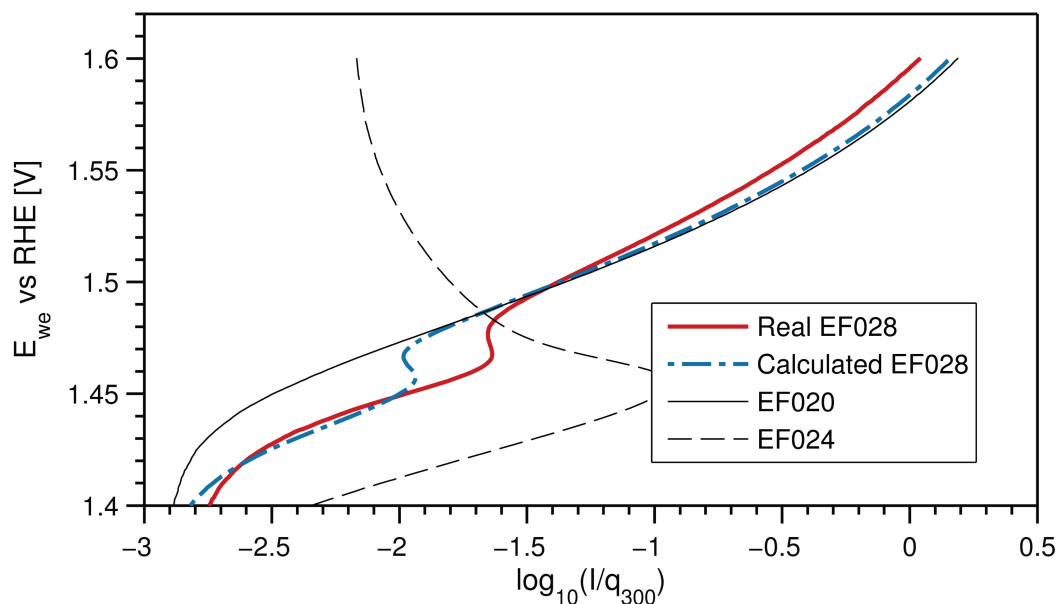
Figure 4.28: Comparison of real and calculated Tafel plots for EF028, the physically mixed catalyst with 6.7 at% ruthenium. Calculated plots are the sum of current contributions from ruthenium (thin dashed line) and iridium (thin solid line) oxides at a given potential, weighted by the composition.

Figure 4.29: Comparison of real and calculated Tafel plots for EF029, the physically mixed catalyst with 14.1 at% ruthenium. Calculated plots are the sum of current contributions from ruthenium (thin dashed line) and iridium (thin solid line) oxides at a given potential, weighted by the composition.
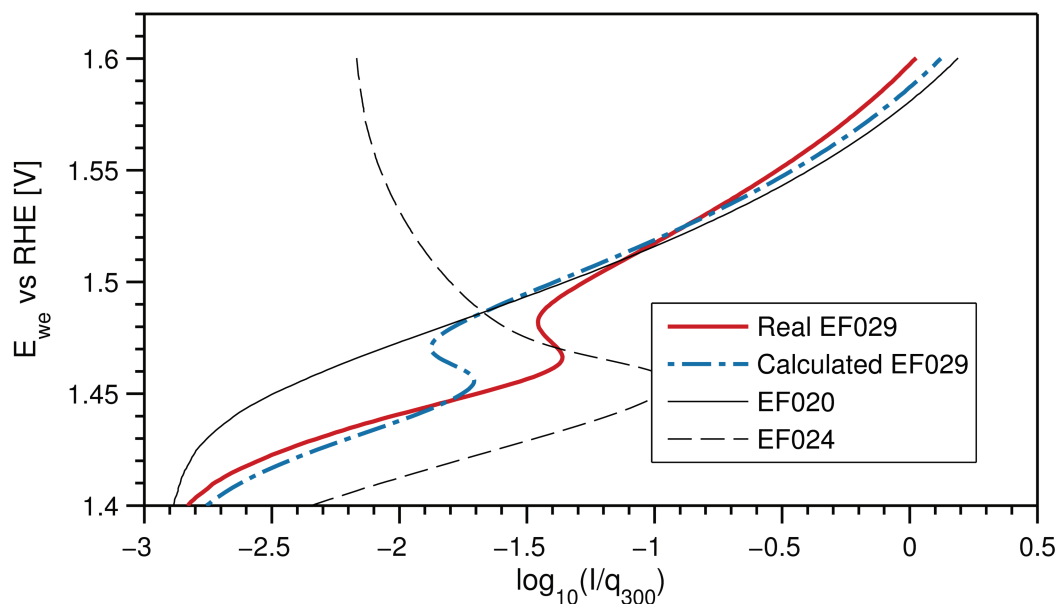
4.4.5   Accelerated stability testing

Figure 4.30 show a comparison from the AST testing of the atomically mixed oxide catalysts. Solid lines represent the linear sweep before the degradation of the catalyst, while dashed lines are for the sweep after the cycling. All samples have a significant activity loss. The ordering is the same after cycling, with higher ruthenium content giving higher activities, but the difference is lower than before. Table 4.8 shows the potential increase at 10 mA/C from the AST cycling.

Table 4.8: Potential increase from AST cycling on atomically mixed oxides at a normalized current of 10 mA/C

Sample	Potential increase [mV]	Percentage increase
EF020	4.6	0.31
EF021	18.2	1.25
EF022	23.5	1.62
EF023	25.8	1.79

Figure 4.31, Figure 4.32 and Figure 4.33 do the same comparison for each pair of atomically and physically mixed oxides with the same ruthenium content. At high currents, the pre-AST activity of the physically mixed sample approaches and even sinks below the post-AST activity of the atomically mixed sample.
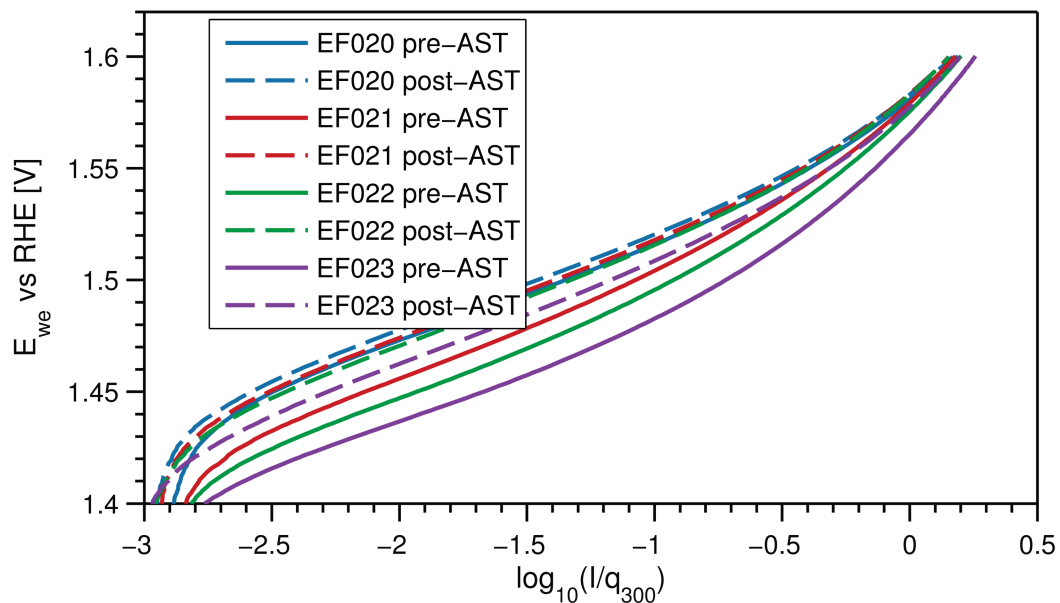
Figure 4.30: Comparisons of the AST-testing of the mixed oxide catalysts. The solid lines are from the linear sweep before the degradation cycling, while the dashed lines are for the sweep after.

Figure 4.31: Comparisons of the AST-testing of the atomically mixed and physically mixed samples with 4.7 at% ruthenium in the catalyst metal. The solid lines are from the linear sweep before the degradation cycling, while the dashed lines are for the sweep after.

Figure 4.32: Comparisons of the AST-testing of the atomically mixed and physically mixed samples with 6.7 at% ruthenium in the catalyst metal. The solid lines are from the linear sweep before the degradation cycling, while the dashed lines are for the sweep after.
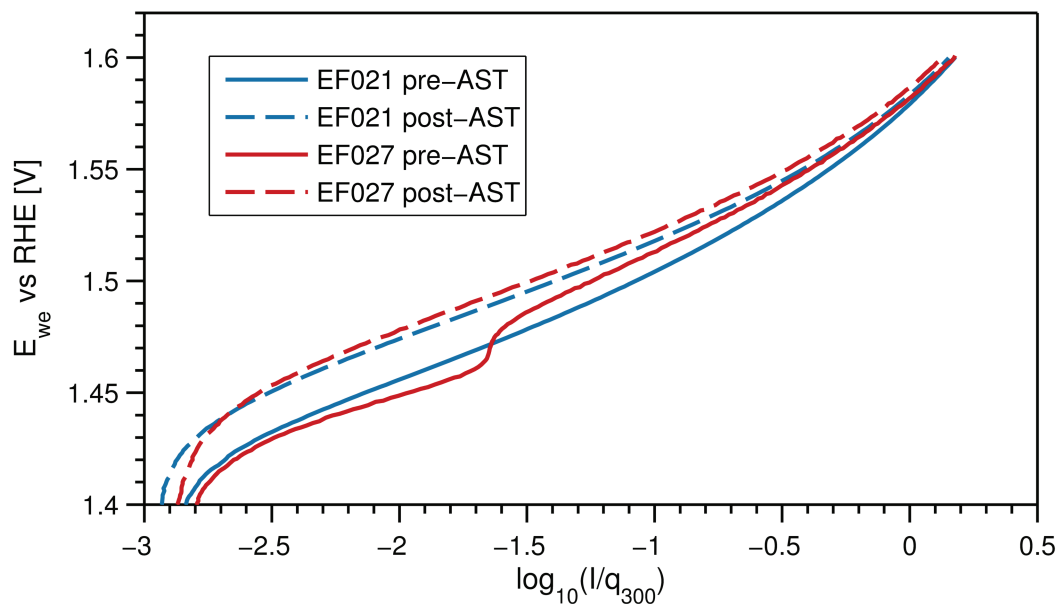

Figure 4.33: Comparisons of the AST-testing of the atomically mixed and physically mixed samples with 14.1 at% ruthenium in the catalyst metal. The solid lines are from the linear sweep before the degradation cycling, while the dashed lines are for the sweep after.
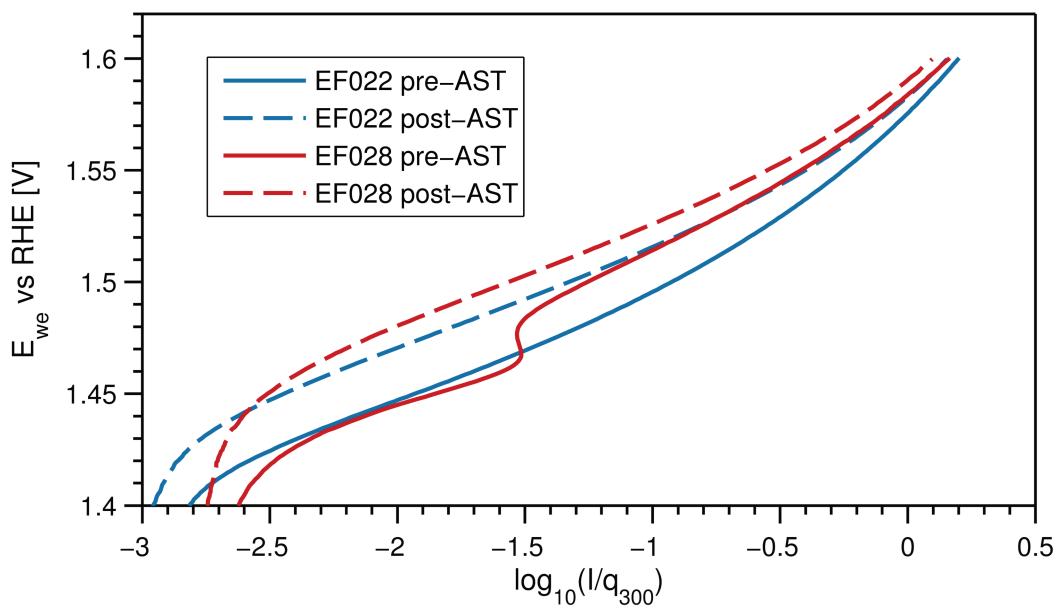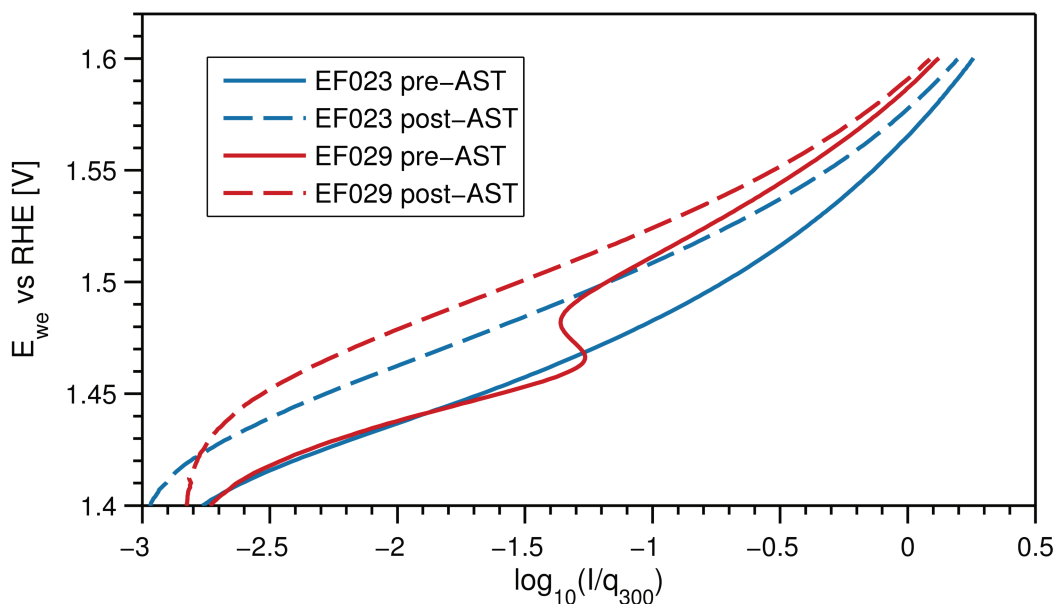
5   Discussion

The results shown in section 1 will be discussed below. The first sections discuss the results regarding the novel synthesis method, continuing on the conclusions of the preliminary project, and extending them using the results of the mixed oxide synthesis. Then the results from electrochemical measurements will be covered, with an emphasis on how the properties depend on the catalyst composition, and relating these results to previous studies.

5.1   Catalyst morphology

The TEM images in section 4.1 shows that the particle morphology of IrO_2/ATO catalyst powders produced by the microwave polyol method is very similar to particles synthesized by the normal polyol method. Both samples show slight agglomeration of catalyst particles and some support areas with little or no catalyst, but the overall morphology looks good. Catalyst particle loading seem to be even, and this is confirmed by TEM images at lower magnifications. The average particle size for the microwave sample is 2.28 nm, while the control sample has a slightly lower size at 2.14 nm. Particle size distributions are narrow, with most particles inside ± 0.6nm of the average diameter.

This confirms the conclusion in the preliminary work, that the microwave polyol synthesis method is indeed a valid alternative to the normal polyol method for producing ATO-supported iridium oxide catalysts, as the catalytic properties and particle morphology are similar.

The synthesis route and parameters used for synthesizing the microwave sample EF018 in the preliminary work were carried on for all the catalyst produced in this work, with a small increase in the starting pH value. This means that the particle morphology should be similar for at least the iridium-rich samples synthesized in this work. TEM imaging was not done for the samples synthesized in this study, so this is unconfirmed. It should be reasonable to assume the morphologies will still be similar, as there was found no significant deviations when comparing the electrochemical results to those of previous studies. For the normal polyol method the morphology have been reported as being constant with the addition of ruthenium [28].

5.2   Mixed oxide synthesis

The EDS measurements and synthesis observations show that the microwave polyol synthesis method, established for pure Ir/ATO catalysts in the preliminary project, have been successfully extended to producing Ru/ATO and mixed oxide catalysts.

The ruthenium contents of the atomically mixed oxide catalysts are not quite up to the target values, but for the pure ruthenium syntheses the catalyst loading on the support was within one standard deviation of the target. All samples produced in this study had good loading values. Target ruthenium loading indicates that this method has a great potential in reducing ruthenium, which have been problematic for the normal polyol method.

In addition to EDS measurements, this study also employed XPS to try to analyze the surface composition of a mixed oxide, as surface segregation has been reported leading to surface enrichment of iridium. This did unfortunately not yield any results significant to be included, due to high measurement uncertainty. The emission volume from XPS is also on the borderline of being able to give any real surface data for particles this small.

A very possible source of the lowered ruthenium content in the mixed oxides is the case of the precursor, $RuCl_3$, not being completely dissolved in ethylene glycol before transferring to the reaction beaker. Some particles were observed to be remaining in the sample jars, and the importance of this was underestimated during the experiment. For the synthesis of pure ruthenium oxide this was taken into consideration, and several steps of dissolution and addition was added to the procedure, using an ultrasonic bath to help dissolve the ruthenium salt. Due to the increased reaction volume, five seconds was added to the initial heating procedure, as the volume influences the dielectric heating during the synthesis.

The EG supernatant color and opacity is another indicator of the successfulness of the synthesis. Both dissolved precursor salt and non-deposited catalyst particles left in the solution after centrifugation will give the solution some color, while pure ethylene glycol itself is colorless. For all the experiments run for this work, the supernatant was clear and nearly colorless; for the ruthenium oxide synthesis the supernatant had a slight green tint. Comparing this with supernatant colors for the normal polyol synthesis for previous studies in this lab [18, 28, 36], the microwave synthesis method seem to be superior in terms of reduction ability and in terms of deposition of the catalyst metal on the support particles.

The flexibility of the synthesis method should also be taken into account. In addition to confirming the hypothesis that the microwave polyol method is faster than the normal polyol method, this study shows how catalyst batches with different compositions may be produced in parallel with great control over the different compositions. As concluded in the preliminary work (see section 2.6.1), this method is faster, due to there being no time expensive heating and deposition steps, and requires less work. In practice, this has saved several days of experimental work in this study.

The sharp pH decrease observed previously was also present in all syntheses in this study. The pH was adjusted to 11 before the heating step (after precursor addition), and dropped down to 1-1.5 after cooling for 2 hours. In order to understand the source of the pH drop, two beakers, one with pure EG and one with ATO dispersed in EG, was treated to the same heating procedure. The results show no significant decrease for pure EG, but the drop was present in the beaker with dispersed ATO. This proves that most of the pH change is due to some reaction between ethylene glycol and the support oxide. The nature of this reaction was not further investigated. In fact, pH levels around 1 have previously been found helpful in depositing catalyst particles on the support surface and avoiding agglomeration, as there will be electrostatic forces acting to repulse the metal particles from each other, and attract metal particles to the support surface, as described in section 2.5.

In any case, this study have shown that microwave polyol synthesis is a favorable method for producing mixed oxides, showing a great potential for reducing ruthenium, and yielding close to target catalyst loading values, in addition to being faster and more flexible than the normal polyol method.

5.3   Effect of ruthenium in mixed oxides

The properties of iridium oxide and ruthenium oxide catalysts may be compared from the voltammograms (Figure 4.7) and polarization curves (Figure 4.19). Both behave as expected from previous studies of these catalysts [5, 36]. The voltammograms for the two have distinctly different shapes, with iridium oxide having an anodic current peak at 1.02 V, and ruthenium oxide at 0.75V. The polarization curves show that the ruthenium oxide has a much higher reaction current than iridium oxide, but the curve bends backwards towards lower currents at a potential of 1.45V. This is due to dissolution of ruthenium due to it being further oxidized and soluble in water, and shows in practice how ruthenium oxide alone is unsuited as a catalyst for the OER due to instability.

There was a significant difference in the charge at 300mV (Table 4.6), with ruthenium oxide having a q_{300} value nearly half that of iridium oxide. Unfortunately, difficulties in the preparation of the working electrodes during this study remove the ability to draw any conclusions from this. It was found that some catalyst dispersions, especially the ruthenium oxide, were hard to deposit evenly on the gold electrode. The catalyst surface area will thus vary between samples. This also signifies the importance of normalizing the voltammetry data in order to eliminate, or at least decrease the importance of, the electrode preparation for the current data in the polarization curves.

From Figure 4.10 it can be seen that the anodic current peaks of the atomic mixes shift towards lower potentials as the ruthenium content increases, and the voltammogram shapes warp slightly towards the shape of ruthenium oxide.

A curious observation from Figure 4.11 is that the anodic current peaks for the physical mixes do not shift as they did for the atomic mixes. The voltammogram shapes seem to follow that of pure iridium oxide. One would expect the shapes to shift like it does for the atomic mixes. No explanation can be offered why this is not the case here.

The figures in section 4.4.2 shows plots of the inverse of the charge as a function of the square root of the sweep rate and charge as a function of the inverse of the square root of the sweep rate. As discussed in section 2.3.4 in the theory these are expected to be linear for larger particles, but as the particles in this study are very small, this is not the case for the catalysts in this study. As extrapolating the functions of these in order to calculate the outer and total charges did not seem to give accurate values, the q_{300} values are used to normalize the experimental current data in this work.

The polarization curves in Figure 4.17 show that, as expected from theory, addition of ruthenium to an iridium oxide catalyst does have a positive effect on the catalytic activity. When the ruthenium content increases, the polarization curves shift towards the right, towards higher currents and lower reaction potentials. Figure 4.19 shows that the same principle applies to physically mixed oxides, which are mixtures made from separate Ir/ATO and Ru/ATO powders. However, for these samples the curves bend upwards at a voltage just above 1.45 V, just like the polarization curve for pure ruthenium oxide.

The dissimilarity of the atomically mixed oxides and their associated physically mixed catalysts signifies that the atomically mixed oxides are indeed single phase atomic mixes, and not separate particles of ruthenium and iridium oxides. If the latter was the case one would expect the polarization curves would be more similar to that of the physically mixed catalysts. As TEM imaging was not performed on these samples, this has not been confirmed by quantitative analysis. The catalyst particle sizes are, however, at the limit of the spatial resolution of EDS measurements in a FEG TEM[37], so it might be challenging to isolate one single particle and prove the presence of both iridium and ruthenium in the same article. Nevertheless, the voltammetry does indicate that is the case.

The ohmic loss compensation of the polarization curves is described in section 4.4.4. In practice this removes the contribution from cell resistance, and allows focusing on the catalytic properties only, by extending the linear region where the reaction dynamics follow the Tafel equation closely. There were some difficulties in fitting equation (2.13) for the physically mixed samples due to the loss of activity. It was only possible to fit the small linear region to the linear part of the equation, where the ohmic loss has little contribution. The fit range is limited by the dashed lines in the plots, which can be viewed in Figure 4.20 and in appendix A. Due to this the ohmic loss plots for these samples should be random instead of linear. For EF029, the physically mixed sample with 14.1 % ruthenium oxide the ohmic loss plot has a wave form, indicating the linear slope is slightly too low. The same is seen for the ruthenium oxide. Unfortunately, this was the best fitting the data and algorithm allowed. When considering the results following from the curve fitting it should be taken into account that this imposes an uncertainty on the data following from the curve fitting.

Plotting the iR compensated current at 1.5 V (Figure 4.23) as a function of the composition shows a linear relationship, supporting the hypothesis of linear superposition of the properties of the components. For the atomic mixes it should be considered that the study by Owe et al. reported surface segregation leading to lowered active ruthenium content, as the ruthenium/iridium ratio is lower on the surface than in the bulk. Practically, this would mean a shift to the left of the data discussed here. Unfortunately, measurement of the exact active surface composition may not be practical for particles of this size.

Plots of the potential at a constant normalized, iR corrected current are presented for three different current densities. The data does supports the hypothesis of linear superposition, as the data points seem to follow closely the line calculated by assuming linear superposition. As the

data points are for a single experiment, no numerical values for the uncertainty in the current values can be offered. The uncertainties in compositional measurements have been established and listed above, but including these seem irrelevant as the composition data from EDS may, as discussed previously, not accurately represent the active surface concentration. The possibility of surface segregation should be kept in mind when considering the data.

The plot of the Tafel slopes (Figure 4.22) shows an interesting property. For the two sets of mixes, atomic and physical, the slope decreases almost linearly with increasing. This is actually the opposite of the relationship found by Kötz and Stucki, but may be able to fit the relationship they propose for the assumption of linear superposition. More data points would be needed to confirm if this is the case.

Figures 4.27-29 show some interesting properties of the physically mixed oxides. The figures plot the polarization curves along with their calculated counterparts, which are linearly weighted superpositions of the polarization curves of iridium and ruthenium oxides, shown in the same figures. It can be seen that the potential at which the activity drops is slightly higher for the experimental polarization curves, meaning there is a very slight stabilization effect even in the physical mixtures of the two catalyst particles.

All in all the results seem to support the hypothesis that the properties of a mixed oxide are linear or near linear superpositions of the properties of its components. At least the interactions between iridium and ruthenium in a mixed oxide are very weak. This deviates from the results found for sputtered oxide films as found by Kötz and Stucki, and supports the results found for annealed oxide particles as found by Owe et al. Addition of even small amounts of ruthenium give a significant increase in catalytic activity compared to a pure ATO-supported iridium oxide catalyst.

5.4   Catalyst stability

Of course, catalytic activity must be considered with regards to the stability of the catalyst. The ruthenium oxide and physical catalyst mixes have already been shown as having very poor stability, with catalytic activity loss happening once the potential at the electrode gets above 1.45V. The atomically mixed oxides do not show this degradation, proving that iridium does have a stabilizing effect on ruthenium in mixed oxides.

Figure 4.30 shows comparisons from the AST testing of the mixed oxide catalysts. Table 4.8 lists numerical values for the potential increase for a normalized current of 10mA/C from the AST cycling. The percent wise potential increase becomes higher as the ruthenium content increases, with the 14.1 at% ruthenium sample having a 1.79% increase. Pure iridium oxide does also have a certain, although low, catalytic activity loss. The ruthenium content is still significant, as the ruthenium rich oxides still have higher catalytic activities, but the difference is lower than before the degradation cycling. In any case, the stabilizing effect of iridium is good enough to have ruthenium remaining after AST cycling.

The plots comparing the AST testing for each pair of atomically and physically mixed oxides show that the pre-AST polarization curves for the physical mixes dip below even the post-AST polarization curves of the associated atomic mix. In fact, as seen by Figure 4.19 they drop even below the activity of pure iridium oxide. This is due to them having less catalyst mass, and confirms that all the ruthenium is gone from the catalyst at the end of the polarization sweep.

6 Conclusions

In this study the microwave polyol method, established as an advantageous route for producing ATO supported iridium oxide in the preliminary work, has been extended to include ruthenium oxide and mixed oxides of iridium and ruthenium. The synthesis route was fast, flexible, and allows for great control when synthesizing catalysts of different compositions in the laboratory. The method is believed to give near full reduction and deposition of both iridium and ruthenium, giving target ruthenium loading, and thus shows greater reduction power than what has been seen recently for the normal polyol method. TEM imaging of previously synthesized catalysts showed that the particle morphology is very similar for catalysts made by the microwave polyol method and the normal polyol method.

This study has synthesized and analyzed ATO-supported catalysts of IrO_2, RuO_2 and both atomically and physically mixed oxides of iridium and ruthenium, the physical mixes being created from the pure oxides, with the same average ruthenium/iridium ratio as the atomically mixed oxides.

Ruthenium has been show to give a significant increase of catalytic activity in mixed oxides with iridium. The atomically mixed oxides were shown to be much more stable than the physically mixed oxides. Physically mixed oxides were found to have the ruthenium oxide dissolve at electrode potentials above 1.45 V, as the case is for pure ruthenium oxide. In the atomically mixed oxide, the ruthenium was stabilized, and was still present and active after AST stability testing.

The catalytic activity of iridium-ruthenium mixed oxide catalysts was found to follow close to the relationship calculated by assuming the total current is a linear superposition of contributions from iridium and ruthenium oxides, indicating that any electronic interactions between ruthenium and iridium are weak. This deviates from what Kötz and Stucki [6] found for sputtered oxide films of the same elements, and supports the results of Owe et al. [5] found for annealed oxide particles.

6.1 Suggestions for further work

It may be interesting to examine the iridium-ruthenium oxide system further. The microwave polyol method allows for faster synthesis of catalysts of different compositions, so it would be easier to make more compositions of the oxide system, both atomic and physical mixes, in order to get more data points on the relationship between catalytic properties and oxide composition. This work has focused on the iridium-rich end of the system.

The catalysts in this study have only been tested on gold electrodes in aqueous test cells, so it would be useful to perform tests on the catalyst in a more real environment using a PEM cell.

7 References

1.   Marshall, A.T., *Electrocatalysts for the oxygen evolution electrode in water electrolysers using proton exchange membranes : synthesis and characterisation*, in *Department of Materials Science and Engineering* 2005, NTNU: Trondheim.

2.   Rand, D.A.J. and R.M. Dell, *Hydrogen energy : challenges and prospects*. 2008, Cambridge: RSC Publ.

3.   Marshall, A., et al., *Hydrogen production by advanced proton exchange membrane (PEM) water electrolysers—Reduced energy consumption by improved electrocatalysis.* Energy, 2007. **32**(4): p. 431-436.

4.   Fanavoll, E., *Catalyst for PEM water electrolysis; A study of the microwave polyol synthesis method for ATO-supported IrO2 catalyst for the oxygen evolution reaction. (preliminary project to master thesis)*, 2012, NTNU: Trondheim.

5.   Owe, L.-E., et al., *Iridium–ruthenium single phase mixed oxides for oxygen evolution: Composition dependence of electrocatalytic activity.* Electrochimica Acta, 2012. **70**(0): p. 158-164.

6.   Kötz, R. and S. Stucki, *Stabilization of RuO2 by IrO2 for anodic oxygen evolution in acid media.* Electrochimica Acta, 1986. **31**(10): p. 1311-1316.

7.   B. V. Tilak, P.W.T.L., J. E. Colman, and S. Srinivasan, *Electrolytic production of Hydrogen.* Comprehensive Treatise of Electrochemistry, 1981. **2**.

8.   Hamann, C.H., A. Hamnett, and W. Vielstich, *Electrochemistry*. 2007, Weinheim: Wiley. XVIII, 531 s. : ill.

9.   Marcelo Carmo, J.M., Detlef Stolten *A review on the recent progress in electrocatalysis of polymer exchange membrane water electrolysis*. World Hydrogen Energy Conference 2012 2012.

10.   Tunold, R., et al., *Materials for Electrocatalysis of Oxygen Evolution Process in PEM Water Electrolysis Cells.* ECS Transactions, 2010. **25**(23): p. 103-117.

11.   Matsumoto, Y. and E. Sato, *Electrocatalytic properties of transition metal oxides for oxygen evolution reaction.* Materials Chemistry and Physics, 1986. **14**(5): p. 397-426.

12.   Trasatti, S., *Electrocatalysis in the anodic evolution of oxygen and chlorine.* Electrochimica Acta, 1984. **29**(11): p. 1503-1512.

13.   Chorkendorff, I. and J.W. Niemantsverdriet, *Concepts of modern catalysis and kinetics*. 2007, Weinheim: Wiley-VCH. XX, 457 s. : ill.

14.   Vojvodic, A. and J.K. Norskov, *Optimizing Perovskites for the Water-Splitting Reaction.* Science, 2011. **334**(6061): p. 1355-1356.

15.   Cheng, J., et al., *Study of IrxRu1–xO2 oxides as anodic electrocatalysts for solid polymer electrolyte water electrolysis.* Electrochimica Acta, 2009. **54**(26): p. 6250-6256.

16.   Suntivich, J., et al., *A Perovskite Oxide Optimized for Oxygen Evolution Catalysis from Molecular Orbital Principles.* Science, 2011. **334**(6061): p. 1383-1385.

17.   Bontempelli, G. and R. Toniolo, *MEASUREMENT METHODS | Electrochemical: Linear Sweep and Cyclic Voltammetry*, in *Encyclopedia of Electrochemical Power Sources*, G. Editor-in-Chief: Jürgen, Editor. 2009, Elsevier: Amsterdam. p. 643-654.

18.   Sandbakk, K.D., *Syntese og karakterisering av katalysatorer for vannelektrolyse: Effekt av bærestrukturer og synteseforhold på den katalytiske aktiviteten*, in *Department of Materials Science and Engineering*2011, NTNU: Trondheim.

19.   Hu, J.-M., J.-Q. Zhang, and C.-N. Cao, *Oxygen evolution reaction on IrO2-based DSA® type electrodes: kinetics analysis of Tafel lines and EIS.* International Journal of Hydrogen Energy, 2004. **29**(8): p. 791-797.

20.   Ardizzone, S., G. Fregonara, and S. Trasatti, *"Inner" and "outer" active surface of RuO2 electrodes.* Electrochimica Acta, 1990. **35**(1): p. 263-267.

21.   Hammer, B., *Special Sites at Noble and Late Transition Metal Catalysts.* Topics in Catalysis, 2006. **37**(1): p. 3-16.

22.   Ruban, A., et al., *Surface electronic structure and reactivity of transition and noble metals.* Journal of Molecular Catalysis A: Chemical, 1997. **115**(3): p. 421-429.

23.   Hammer, B. and J.K. Nørskov, *Theoretical surface science and catalysis—calculations and concepts*, in *Advances in Catalysis*, H.K. Bruce C. Gates, Editor. 2000, Academic Press. p. 71-129.

24.   Schlapka, A., et al., *Surface Strain versus Substrate Interaction in Heteroepitaxial Metal Layers: Pt on Ru(0001).* Physical Review Letters, 2003. **91**(1): p. 016101.

25.   H. Hei, et al., *Controlled Synthesis and Characterization of Nobel Metal Nanoparticles.* Soft Nanoscience Letters, 2012. **2**(3).

26.   Bonet, F., et al., *Synthesis of monodisperse Au, Pt, Pd, Ru and Ir nanoparticles in ethylene glycol.* Nanostructured Materials, 1999. **11**(8): p. 1277-1284.

27.   Bock, C., et al., *Size-Selected Synthesis of PtRu Nano-Catalysts: Reaction and Size Control Mechanism.* Journal of the American Chemical Society, 2004. **126**(25): p. 8028-8037.

28.   Cacciuttolo, Q., *Study of supported catalyst for oxygen evolution reaction in water electrolysis*, in *Chimie Paris*2011, ParisTech.

29.   Anumol, E.A., et al., *New Insights into Selective Heterogeneous Nucleation of Metal Nanoparticles on Oxides by Microwave-Assisted Reduction: Rapid Synthesis of High-Activity Supported Catalysts.* ACS Nano, 2011. **5**(10): p. 8049-8061.

30.   Chu, Y.-Y., et al., *Performance of Pt/C catalysts prepared by microwave-assisted polyol process for methanol electrooxidation.* Journal of Power Sources, 2010. **195**(7): p. 1799-1804.

31.   Harish, S., et al., *Microwave assisted polyol method for the preparation of Pt/C, Ru/C and PtRu/C nanoparticles and its application in electrooxidation of methanol.* Journal of Power Sources, 2012. **214**(0): p. 33-39.

32.   Lebègue, E., S. Baranton, and C. Coutanceau, *Polyol synthesis of nanosized Pt/C electrocatalysts assisted by pulse microwave activation.* Journal of Power Sources, 2011. **196**(3): p. 920-927.

33.   Song, S., Y. Wang, and P.K. Shen, *Pulse-microwave assisted polyol synthesis of highly dispersed high loading Pt/C electrocatalyst for oxygen reduction reaction.* Journal of Power Sources, 2007. **170**(1): p. 46-49.

34.   Li, X., et al., *Microwave polyol synthesis of Pt/CNTs catalysts: Effects of pH on particle size and electrocatalytic activity for methanol electrooxidization.* Carbon, 2005. **43**(10): p. 2168-2174.

35.   Patel, K., et al., *Synthesis of Pt, Pd, Pt/Ag and Pd/Ag nanoparticles by microwave-polyol method.* Journal of Chemical Sciences, 2005. **117**(4): p. 311-316.

36.   Gurrik, S., *Performance of supported catalysts for water electrolysis*, in *Department of Materials Science and Engineering* 2012, NTNU: Trondheim.

37.   *Energy dispersive X-ray (EDS) microanalysis of thin specimens in the analytical electron microscope* Central Facility for Advanced Microscopy and Microanalysis

Appendix A: iR correction of polarization curves
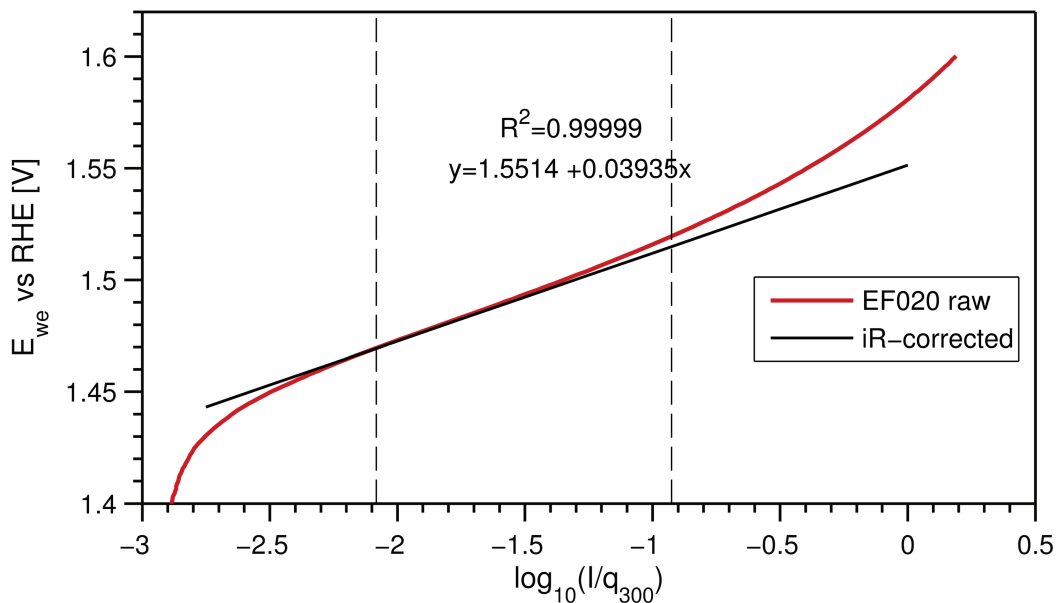
Figure A.1: Approximation of the linear region in the Tafel plot of EF020. The data for the linear approximation are found by fitting equation (2.13) to the experimental data by the Levenberg Marquardt algorithm. The dashed lines mark the region where the fit was performed.
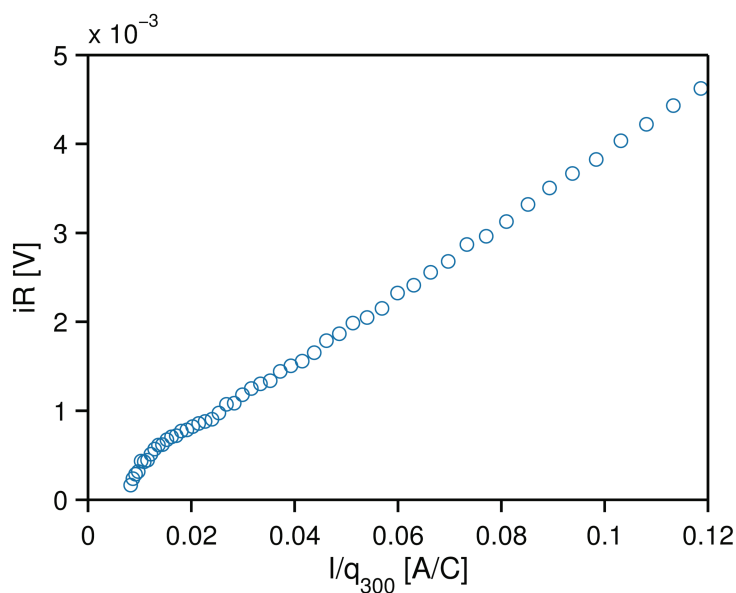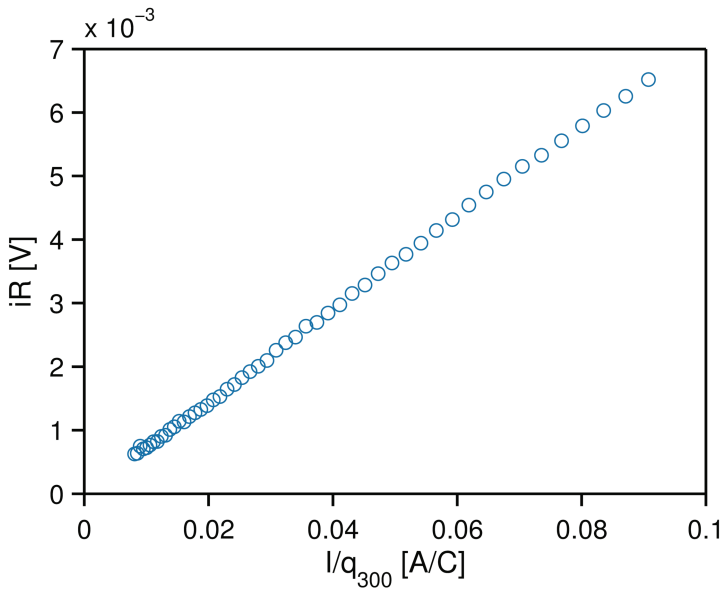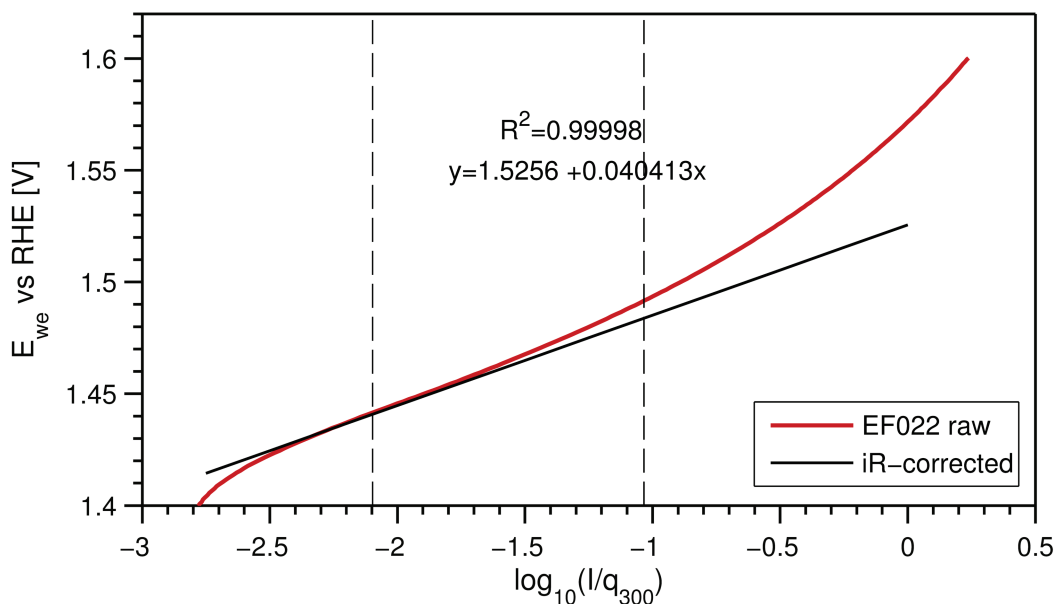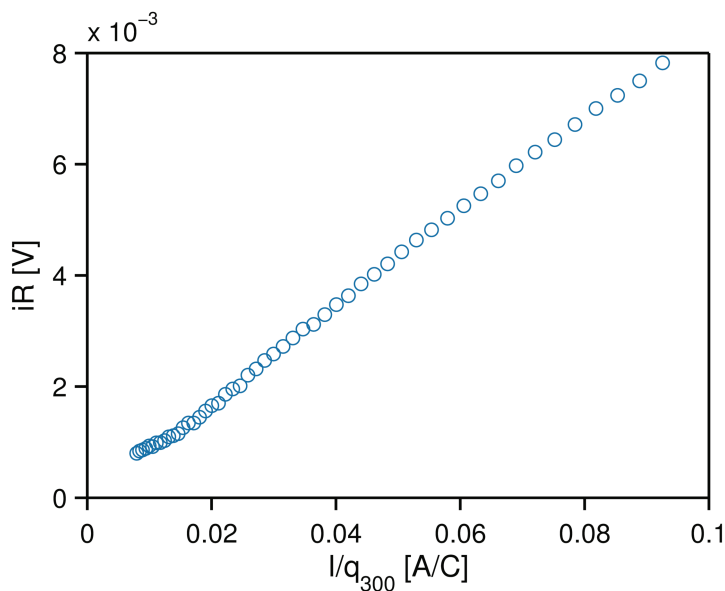

Figure A.2: Uncompensated ohmic loss for EF020, calculated as the difference between the raw data and the linear approximation.
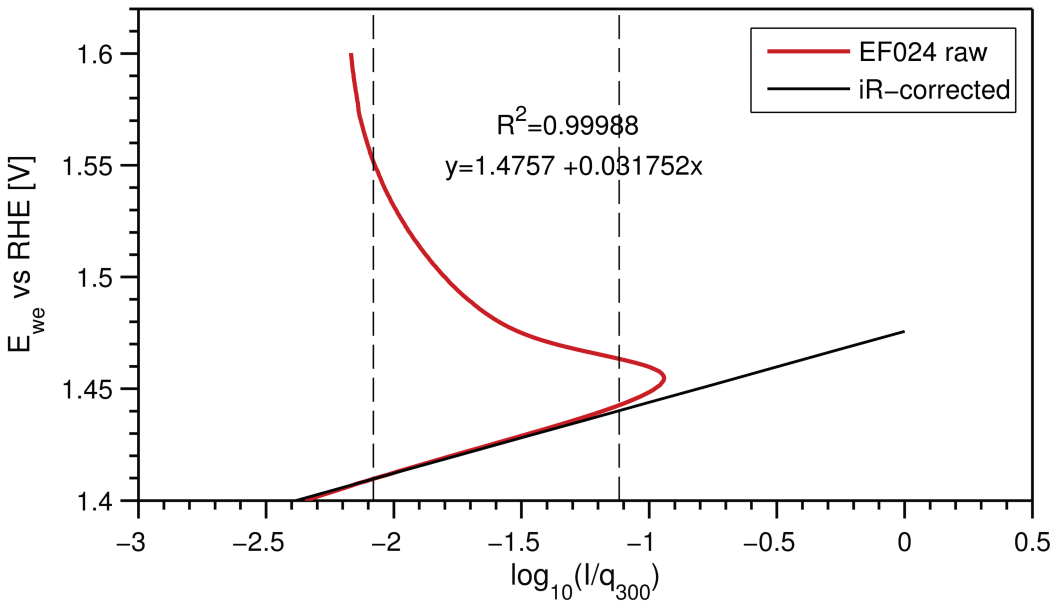
Figure A.3: Approximation of the linear region in the Tafel plot of EF021. The data for the linear approximation are found by fitting equation (2.13) to the experimental data by the Levenberg Marquardt algorithm. The dashed lines mark the region where the fit was performed.
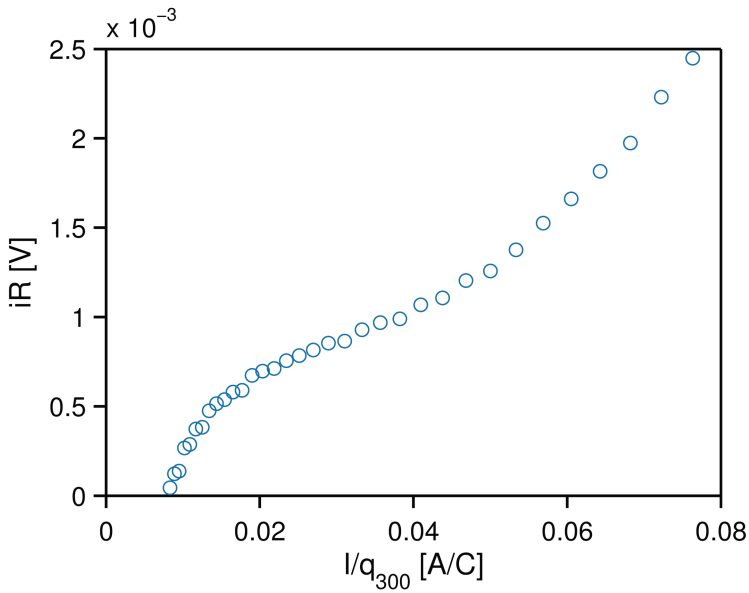

Figure A.4: Uncompensated ohmic loss for EF021, calculated as the difference between the raw data and the linear approximation.

Figure A.5: Approximation of the linear region in the Tafel plot of EF022. The data for the linear approximation are found by fitting equation (2.13) to the experimental data by the Levenberg Marquardt algorithm. The dashed lines mark the region where the fit was performed.

Figure A.6: Uncompensated ohmic loss for EF022, calculated as the difference between the raw data and the linear approximation.
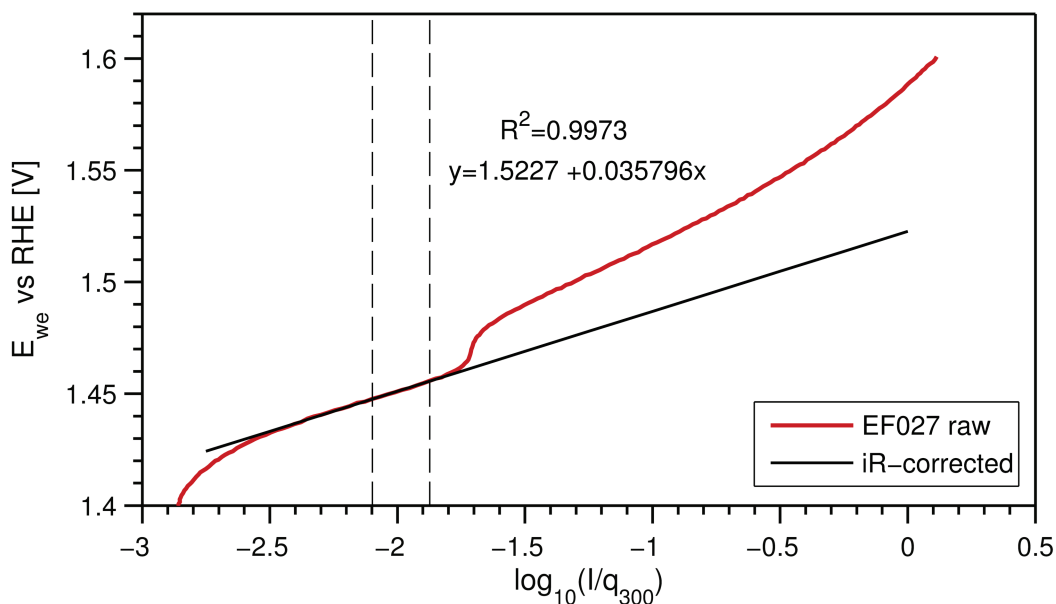
Figure A.7: Approximation of the linear region in the Tafel plot of EF024. The data for the linear approximation are found by fitting equation (2.13) to the experimental data by the Levenberg Marquardt algorithm. The dashed lines mark the region where the fit was performed.

Figure A.8: Uncompensated ohmic loss for EF024, calculated as the difference between the raw data and the linear approximation.

Figure A.9: Approximation of the linear region in the Tafel plot of EF027. The data for the linear approximation are found by fitting the Tafel equation (2.11) to the experimental data by the Levenberg Marquardt algorithm. The dashed lines mark the region where the fit was performed.
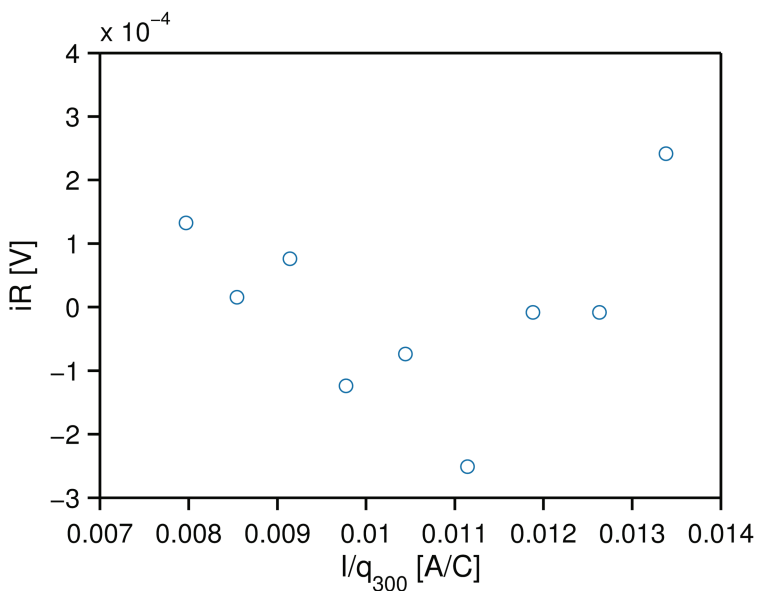

Figure A.10: Uncompensated ohmic loss for EF027, calculated as the difference between the raw data and the linear approximation.
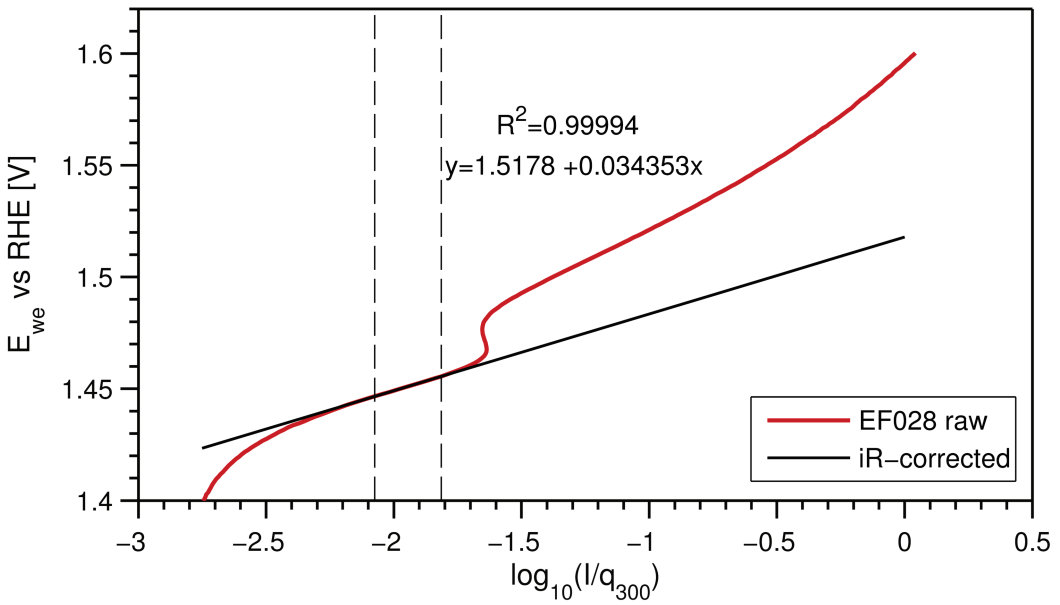
Appendix A: iR correction of polarization curves

Figure A.11: Approximation of the linear region in the Tafel plot of EF028. The data for the linear approximation are found by fitting the Tafel (2.11) to the experimental data by the Levenberg Marquardt algorithm. The dashed lines mark the region where the fit was performed.
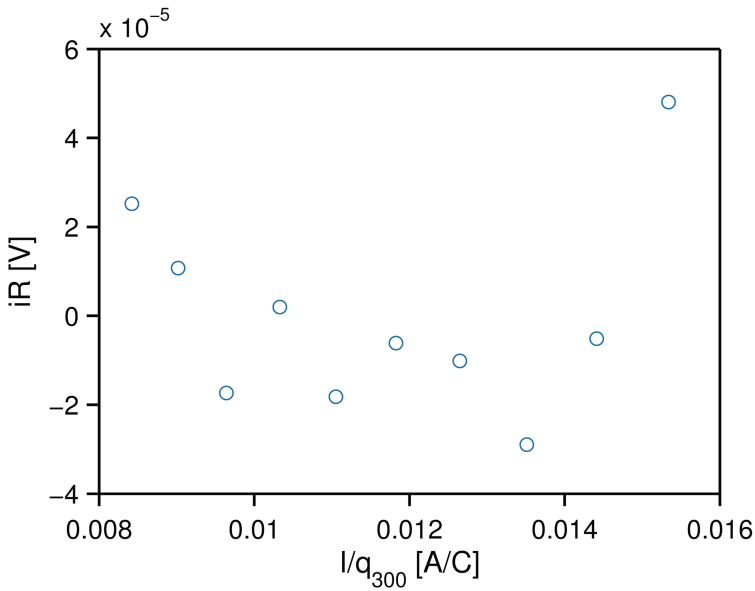

Figure A.12: Uncompensated ohmic loss for EF028, calculated as the difference between the raw data and the linear approximation.
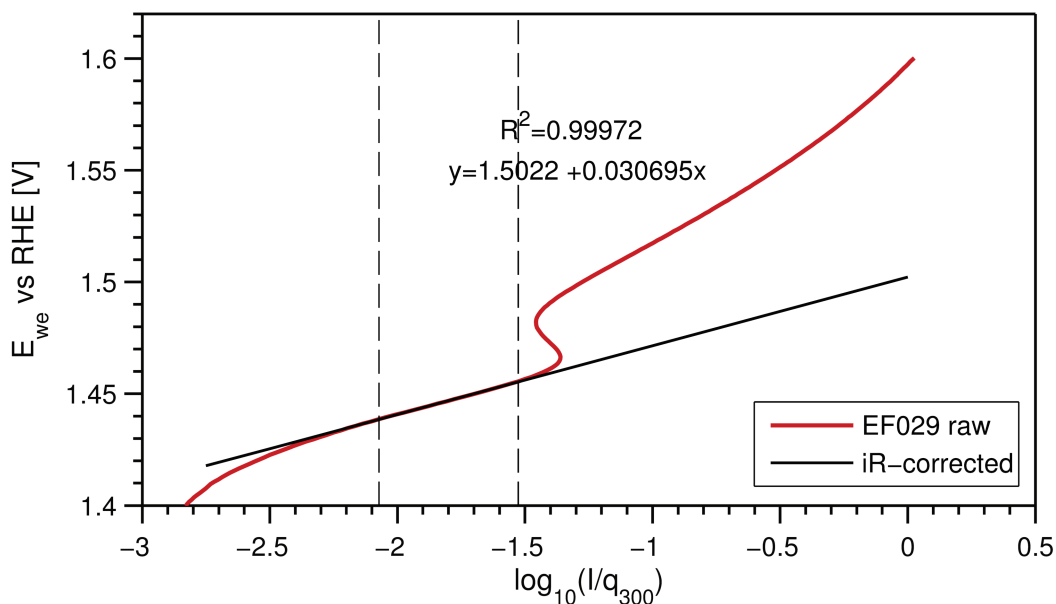
Figure A.13: Approximation of the linear region in the Tafel plot of EF029. The data for the linear approximation are found by fitting the Tafel equation (2.11) to the experimental data by the Levenberg Marquardt algorithm. The dashed lines mark the region where the fit was performed.
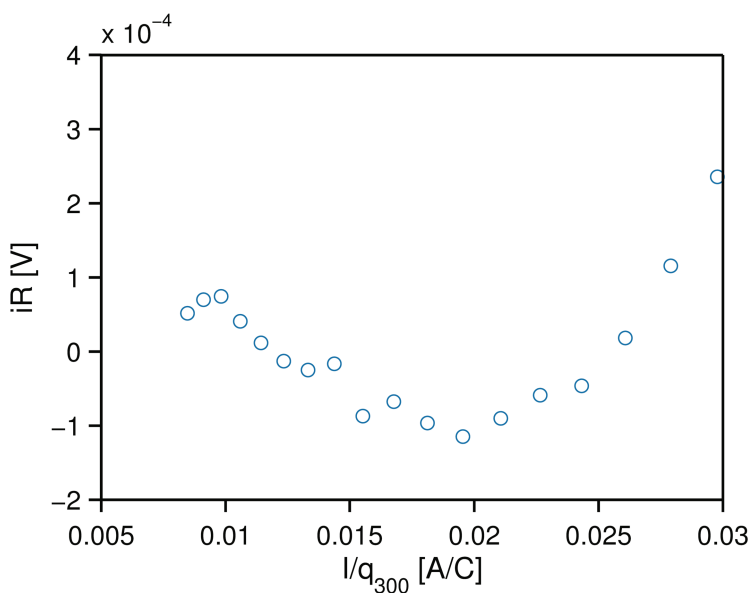

Figure A.14: Uncompensated ohmic loss for EF029, calculated as the difference between the raw data and the linear approximation.